Control Engineering Practice 146 (2024) 105883

Contents lists available at ScienceDirect

Control Engineering Practice

journal homepage: www.elsevier.com/locate/conengprac

An energy efficient fault-tolerant controller for homing of underactuated AUVs☆,☆☆

Cristina Cerrada [a,*], Dictino Chaos [a], David Moreno-Salinas [a], António Pascoal [b], Joaquín Aranda [a]

[a] Department of Computer Science and Automatic Control, National Distance Education University (UNED), C/ Juan del Rosal 16, Madrid, 28040, Spain
[b] Institute for Systems and Robotics, Instituto Superior Técnico, Av. Rovisco Pais 1, Lisbon, 1049-001, Portugal

ARTICLE INFO

Keywords:
AUV
Fault-tolerant control
Optimal control
Fourier series
Energy consumption
Homing

ABSTRACT

In the event of a failure that will prevent an Autonomous Underwater Vehicle (AUV) from executing a specified task, the vehicle must be recovered safely to avoid further damage to itself or to other vehicles/agents in the neighbourhood. Motivated by this operational requirement, this work presents an optimal fault-tolerant controller to drive an underactuated AUV to a recovery point (so-called automatic homing manoeuvre). The case of a critical failure that leaves only one of two stern thrusters available to drive it to the desired recovery area is considered. The control law proposed relies on the use of a Fourier series-based strategy to compute the control action as a function of the relative orientation of the vehicle with respect to the target recovery point. Energy consumption is also considered in the proposed control law, so that an appropriate trade-off can be achieved between reaching the destination faster and reducing the energy consumed as a function of mission requirements and vehicle specifications. The stability and convergence of the proposed scheme are demonstrated analytically, a comparison with MPC scheme is shown and simulation examples illustrate how the control law effectively drives the vehicle to a neighbourhood of the desired target point even in the presence of unknown constant currents.

1. Introduction

In recent years, Autonomous Underwater Vehicles (AUVs) have played a crucial role in the field of ocean exploration, performing multiple missions for both scientific research and industrial applications (Mondal & Banerjee, 2019), thus becoming key tools for the discovery of natural resources and preserve marine life. These vehicles are flexible, efficient and increasingly cost-effective (Yang et al., 2021). Such characteristics allow AUVs to carry out effectively and accurately multiple tasks, such as inspection, exploration, mapping, and monitoring of marine environments and critical underwater infrastructures, target localisation and tracking, and collaborative tasks in the case of complex missions that require the operation of multiple vehicles (Crasta et al., 2018; Ghabcheloo et al., 2009; Glaviano et al., 2022; Moreno-Salinas et al., 2016; Pinto et al., 2021).

Reliable operation of AUVs is critical. If a failure occurs in any of the AUV systems, the integrity of the vehicle may be put at risk, leading to a possible loss of the AUV or endangering humans and animals and even posing a threat to the environment. For these reasons, fault-tolerant systems, which include those responsible for fault detection, fault isolation, and fault accommodation (Podder & Sarkar, 2001) are of special interest within this field. The present work is focused on fault accommodation, which determines the actions or controls to be implemented to contain a given failure. In this context, the minimisation of energy consumption is also of utmost importance since these kinds of vehicles should work autonomously over extended periods of time. Motivated by these considerations, this work proposes an optimal control law to be executed in case of thruster failure to drive the vehicle to a recovery point that allows for a trade-off between energy consumption and reaching the recovery point faster.

Diverse approaches and solutions have been explored in the literature regarding fault accommodation in the event of a thruster failure for Unmanned Marine Vehicles (UMVs), which include AUVs. Most works

☆ This research was funded by project NAUTILUS PID2020-112502RB-C44 by Ministerio de Ciencia e Innovación of Spain. The work of the fourth author was funded by project LARSyS UIDB/50009/2020 and project DRI/ I-P 0699/2020 by Fundação para a Ciência e Tecnologia, and by projects EU FET RAMONES 101017808 and EU ECOBOTICS.SEA 824043 by European Commission.

☆☆ The authors gratefully acknowledge the technical support and access to the simulator provided by the DSOR-ISR group of the Instituto Superior Técnico of the University of Lisbon.

* Corresponding author.
E-mail addresses: criscerrada@dia.uned.es (C. Cerrada), dchaos@dia.uned.es (D. Chaos), dmoreno@dia.uned.es (D. Moreno-Salinas), antonio@isr.tecnico.ulisboa.pt (A. Pascoal), jaranda@dia.uned.es (J. Aranda).

https://doi.org/10.1016/j.conengprac.2024.105883
Received 26 September 2023; Received in revised form 6 February 2024; Accepted 7 February 2024

consider the existence of redundant thrusters along with allocation policies to distribute the force requirements among the remaining thrusters (Baldini et al., 2018; Rauber et al., 2012; Sarkar et al., 2002) or resort to the reconfiguration of the thrusters layout (Pugi et al., 2018). Others approaches used to compensate for this failure are, for example, sliding mode control in Corradini et al. (2011), Hao et al. (2021) and Lv et al. (2020), adaptive fuzzy sliding mode tracking controller for Takagi–Sugeno in Wang et al. (2020), iterative learning algorithm based on a Linear Extended States Observer (LESO) in Hou et al. (2022), and Model Predictive Controller (MPC) in Ding and Zhu (2020). Further references can be consulted in Amin and Hasan (2019). It is relevant to mention Chaos et al. (2022) since, in contrast to previous references, this work considers the extreme situation of controlling an underactuated AUV in the horizontal plane that suffers a critical failure that drastically reduces its Degrees Of Freedom (DOF) and leaves the vehicle with only one thruster available. The solution proposed consists of switching between two control actions that allow the vehicle to be driven in a desired direction, following a spiral-like path. This limited mobility scenario is also considered in the present work, but the solution proposed departs considerably from that advanced in Chaos et al. (2022), as the control law is continuous rather than discontinuous and it allows for a proper trade-off between energy consumption and reaching the recovery point faster.

Optimal control is closely linked to fault-tolerant control. Some of the algorithms typically used to determine optimal fault-tolerant controllers are Particle Swarm Optimisation (PSO) and all its variants (Tian et al., 2022; Zhang & Zhu, 2021), Simulated Annealing (SA) (Ahmadzadeh et al., 2014; Pearson et al., 2001), and Genetic Algorithms (GA) (Cerrada et al., 2023), to name but a few.

As mentioned above, energy consumption is also a critical factor to be taken into account in the control law design. For example, in Xia et al. (2022) the rudder angle control directly affects energy consumption, and a weight coefficient is introduced in the optimisation to adaptively adjust trajectory tracking performance or energy consumption, although the model presented is not valid for the AUV used in the present work, which uses thrusters instead of rudders. Likewise, Yao et al. (2019) deal with energy consumption reduction using MPC based on the state space model of an overactuated AUV for trajectory tracking control and adds a quadratic energy consumption term into the cost function. In Wang et al. (2016) a Liner-Quadratic Regulator (LQR) controller is proposed to stabilise pitch angle and heave motion, and decrease the energy consumption where the parameters are optimised using GA, but no explicit energy consumption data is presented. Sarkar et al. (2015) and Sarkar et al. (2016) design a controller based on sliding mode techniques in connection with Euler–Lagrange based classical optimal control to accomplish optimal energy consumption while tracking a path accurately. In addition, Pedro et al. (2015) define a model for energy consumption to describe the longitudinal drag force and the drag torque, considering these efforts the most influential in energy consumption while the vehicle is moving. It is also important to highlight the work reported in Häusler (2015), Saback et al. (2016) and Wang et al. (2023). Häusler (2015) developed a detailed energy consumption model for an AUV that takes explicitly into account its propulsion system (DC motor + thrusters with propellers) and hydrodynamic drag. The model is used to estimate the energy spent in the execution of a trajectory and is therefore a key ingredient in the computation of an energy-optimal strategy for the vehicle to execute a desired task. Wang et al. (2023) also developed a detailed energy consumption model, but the vehicle differs from the AUV used in the present work because it has a wing, a rudder and a propeller in the tail. Previous work does not take into account the possibility of thruster failure; however, Saback et al. (2016) explore the optimisation of a fault-tolerant control allocation technique together with energy consumption, for an overactuated AUV. The square of thruster forces is used to minimise the thrusters' energy consumption, but the energy consumption results are not shown explicitly.

It is against this background of ideas that in this work, taking as a basis Cerrada et al. (2023), Chaos et al. (2022), and Häusler (2015), the design of an optimal control law for an AUV that minimises the integral square error of the vehicle's trajectory with respect to a desired final position while minimising energy consumption is studied. The vehicle under consideration is an underactuated AUV operating in 2D that suffers a failure in one of its two stern horizontal thrusters, leaving it with only one operational thruster. This failure results in a drastic reduction of the vehicle's mobility, and therefore of its DOF. In this situation, designing and implementing a control scheme that is capable of driving the vehicle to a desired target point is challenging, since if a constant control action is applied to the available thruster, the vehicle will remain turning in circles. Therefore, the proposed control scheme exploits the vehicle's ability to rotate with different radii depending on the magnitude of the control action applied to the remaining thruster. With the appropriate sequence of control actions, which depend on the orientation of the vehicle with respect to the target point, it is possible to drive the vehicle in the desired direction along a spiral-like trajectory. Moreover, a smooth sequence of control actions is required to prevent further damage to the vehicle.

In this critical failure situation, it is of utmost importance to monitor and control the availability of energy in the vehicle's batteries because it could be the case that the theoretically fastest path would consume more energy than that stored in the batteries. Because only one thruster is available, the vehicle cannot manoeuvre in a straight line, and that is why it takes longer and consumes more energy to execute the manoeuvre, than if both thrusters were operational. Therefore, a compromise between speed of convergence to the destination point and energy consumption is necessary. To the best of the authors' knowledge, a similar control design problem for an underactuated vehicle with such an important and critical failure, while taking into account energy consumption, has not been previously addressed.

In order to solve the above challenges, a continuous control law based on Fourier Series is proposed, which provides a smooth sequence of control actions, as desired. The proposed control law also allows for a trade-off between reaching the desired point faster and minimising energy consumption. The choice of the most appropriate control strategy in the event of this critical failure is made according to the importance (weight) assigned to each of the objectives included in the fitness function, allowing for the best solution to be chosen according to the amount of energy for propulsion available on-board.

The main contributions of the work are fourfold:

1. Development of a fault-tolerant control law based on Fourier series to drive an underactuated vehicle with only one thruster working to a desired target point. Due to the risky situation studied, in which the vehicle has limited control actions and movement capabilities, a smooth control law is defined that allows the vehicle to be recovered without further damage or loss.
2. In the scenario considered the control of the remaining energy in the batteries is critical to ensure that the vehicle can reach the recovery point. For this reason, an analysis of the energy consumption model of the vehicle when using a single thruster has been developed. Additionally, the Fourier series parameters have been optimised not only looking for the smoothness of the control law, but also considering the energy consumption.
3. The study of the trade-off solutions between reaching the desired target point as fast as possible and minimising the energy consumed. The trade-off solutions are computed by the weighted sum of two cost functions, energy and ISE (Integral Squared Error). The control law is selected by resorting to Pareto optimisation, where the speed and time of convergence to the desired area depend on the energy stored in the batteries.
4. Analytical demonstration of the stability of the proposed control law together with a proof of convergence of the resulting trajectory to a neighbourhood of the desired target point from any initial condition.

Fig. 1. MEDUSA Class AUV.

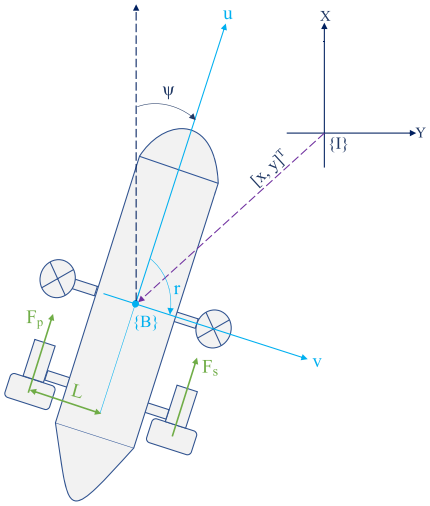

Fig. 2. Inertial and body frames of the AUV.

5. Comparison of the proposed control scheme with MPC scheme to demonstrate the effectiveness of the proposed control. As there is no similar work in the literature and the MPC scheme has been used both in fault-tolerant control and energy consumption minimisation, this method is the best candidate for comparison.

The article is organised as follows. Section 2 introduces the key background material and methodology adopted, and formulates the problem that is central to this work in a rigorous manner. Section 3 offers a proof of stability and convergence of the control strategy derived. In Section 4, the computation of the optimal control law and simulations considering different conditions and constant currents are shown. These results are analysed and discussed in Section 5. The main conclusions are summarised in Section 6.

2. Materials and methods

The vehicle considered is the underactuated MEDUSA Class AUV (Abreu et al., 2016), composed of two torpedo shaped bodies, two stern horizontal thrusters to control surge speed and yaw rate, and two vertical thrusters to control depth and roll, see Fig. 1. The vehicle has been designed with positive buoyancy, which means that in case of failure, it will emerge to the sea surface without the need of additional control actions. Therefore, the fault-tolerant control law is studied for the case where the AUV moves at the surface in a 2D horizontal plane.

2.1. Notation and vehicle's model

Two reference frames are used to define the vehicle's model: the body-frame {B} and the inertial one {I} (Fig. 2). Both frames follow the standard convention adopted in SNAME (SNAME, 1950). The origin of the AUV body-frame is placed at its centre of mass and the speeds of the vehicle expressed in this frame are $\nu = [u; v; r]^T$, where u is surge speed, v is sway speed, and r is yaw rate. The speeds in the inertial frame are $\mathbf{V} = [\dot{x}; \dot{y}; \dot{\psi}]^T$, where the dot indicates the time derivative of a variable so that $\dot{x}$ is the speed along X-axis, $\dot{y}$ is the speed along the Y-axis, ψ is the angle that the vehicle orientation forms with the X-axis, and $\dot{\psi}$ is yaw rate. Hence, based on the above considerations and in the absence of ocean currents, the kinematic model of the vehicle is given by

$$\dot{x} = u \cdot \cos(\psi) - v \cdot \sin(\psi), \tag{1}$$

$$\dot{y} = u \cdot \sin(\psi) + v \cdot \cos(\psi), \tag{2}$$

$$\dot{\psi} = r. \tag{3}$$

For operations in 2D scenarios, the vehicle is controlled by the two stern horizontal thrusters, whose inputs a_s and a_p are the angular velocity references for the starboard and portside thruster propellers, respectively. These inputs are given in terms of standard dimensionless reference commands for the internal controller of the propellers in the non-dimensional range $[-100, 100]$. To obtain the true propeller rotations, a conversion from the non-dimensional commands is needed, e.g. the portside propeller rotational velocity (in rad/s) w_p is computed through the portside propeller rotational velocity n_p (in rps) that depends on a_p and on the maximum propeller rotational velocity n_{max} (in rps), see Eqs. (4)–(5). Similarly, the starboard propeller rotational velocity could be calculated.

$$n_p = n_{max} \cdot a_p/100, \tag{4}$$

$$w_p = 2 \cdot \pi \cdot n_p. \tag{5}$$

Each propeller produces a thrust whose magnitude is proportional to the square of its own angular velocity and its sign is the same as the angular velocity. Thus, the thrust is positive (pushes forward) if control action is positive and negative (pushes backward) if the control action is negative. In accordance, the forces produced in response to the command references are described by

$$F_s(a_s) = K \cdot |a_s| \cdot a_s, \tag{6}$$

$$F_p(a_p) = K \cdot |a_p| \cdot a_p, \tag{7}$$

where K is the proportional constant that relates the command references to the force produced. The total force applied to the vehicle results from the summation of the forces of both thrusters $F = F_p(a_p) + F_s(a_s)$, which also produces the torque $\tau = L \cdot (F_p(a_p) - F_s(a_s))$, where L is the distance of each of the thrusters to the symmetry axis of the vehicle, see Fig. 2.

As mentioned above, the problem under study is the one in which one of the thrusters has been damaged and cannot be operated. Without loss of generality, the starboard thruster has been selected as the faulty one. In this case, only the portside thruster is active and generates the total force and moment $F = F_p(a_p)$ and $\tau = L \cdot F_p(a_p)$, respectively, allowing only for partial control of the surge speed and yaw rate. According to Aguiar and Pascoal (2001), Fossen (2002) and taking into account the particularities of the case study, the dynamic model is rewritten as

$$m_u \cdot \dot{u} - m_v \cdot v \cdot r + D_u(u) \cdot u = F = F_p(a_p), \tag{8}$$

$$m_v \cdot \dot{v} + m_u \cdot u \cdot r + D_v(v) \cdot v = 0, \tag{9}$$

Table 1
List of symbols used in the AUV model.

Symbol	Description
ψ	Angle of orientation of the AUV with respect to the X-axis
$\boldsymbol{\nu} = [u; v; r]^T$	Vehicle's speeds in body-frame: surge, sway and yaw rate
$\mathbf{V} = [\dot{x}; \dot{y}; \dot{\psi}]^T$	Vehicle's speeds in inertial frame: speed along X-axis, speed along the Y-axis and yaw rate
a_s, a_p, a_{pmax}, a_{pmin}	Angular velocity references for the starboard and portside thrusters and upper and lower limits for portside thruster reference
$F_s(a_s)$, $F_p(a_p)$, F, τ	Forces produced by starboard and portside thrusters, total force, and torque
K, L	Proportional constant of the thrusters and distance from the thrusters to the vehicle's symmetry axis
m_u, m_v, m_{uv}, m_r	Mass and inertia constants
$D_u(u)$, $D_v(v)$, $D_r(r)$	Hydrodynamic damping terms
X_u, $X_{\|u\|}$, Y_v, $Y_{\|v\|}$, N_r, $N_{\|r\|}$	Hydrodynamic coefficients

$$m_r \cdot \dot{r} - m_{uv} \cdot u \cdot v + D_r(r) \cdot r = \tau = L \cdot F_p(a_p), \tag{10}$$

where m_u, m_v and m_r are the mass and inertia constants that take into account so-called added masses, and $m_{uv} = m_u - m_v$. Due to the rotation of the body-frame, the Coriolis terms appear as $v \cdot r$, $u \cdot r$, and $u \cdot v$. Finally, the terms $D_u(u)$, $D_v(v)$, and $D_r(r)$ are produced by the dissipating forces of the water, defined as

$$D_u(u) = -X_u - X_{|u|} \cdot |u|, \tag{11}$$

$$D_v(v) = -Y_v - Y_{|v|} \cdot |v|, \tag{12}$$

$$D_r(r) = -N_r - N_{|r|} \cdot |r|, \tag{13}$$

where $X_u, X_{|u|}, Y_v, Y_{|v|}, N_r, N_{|r|}$ are the hydrodynamic coefficients, which are negative and $D_u(u)$, $D_v(v)$ and $D_r(r)$ are positive.

For quick reference, the symbols used in the AUV model are collected in Table 1.

2.2. Problem formulation and control law

In the scenario considered, an underactuated AUV (MEDUSA class vehicle) has suffered a failure and only one of the stern horizontal thrusters is in operational conditions. Therefore, the goal is to execute an automatic homing manoeuvre, which consists of driving the AUV to the neighbourhood of a desired recovery point, by using only this horizontal thruster, i.e., by using a single motor. The recovery point must be reached considering both the integral square error of the vehicle's trajectory and the energy consumed.

For the sake of simplicity of notation, the vehicle's state is defined as $\chi = [x, y, \psi, u, v, r]^T$, with dynamics described by $\dot{\chi} = f(\chi, a_p)$ according to Eqs. (1)–(3), (7)–(10), where a_p is the available control action. Thus, χ_0 is the initial condition, which, without loss of generality, is bounded within the region

$$\Omega = \left\{ \chi \mid x^2 + y^2 \leq R_0^2,\ \boldsymbol{\nu} = 0 \right\} \tag{14}$$

where R_0 is the radius that defines the area of initial conditions.

A neighbourhood Ω_r of the recovery point $\boldsymbol{X_r} = [x_r, y_r]^T$ is defined as

$$\Omega_r = \left\{ \chi \mid (x - x_r)^2 + (y - y_r)^2 < R_f^2 \right\}$$

where R_f is the radius of the neighbourhood which the AUV must reach in finite time t_f and remain there until the final recovery time T_f, there is

$$(x(t) - x_r)^2 + (y(t) - y_r)^2 < R_f^2 \quad \forall\ t_f \leq t \leq T_f. \tag{15}$$

All variables used and explained throughout the Section are listed in Table A.7 of Appendix A for the reader's reference.

In general, the fault-tolerant control law can be considered as a function of time, $t_i = i \cdot \Delta T$, where ΔT is the sampling period, the vehicle's state, $\chi_i = \chi(t_i)$, and a vector θ containing the coefficients that parameterise the control law, as follows,

$$a_p(t_i) = g(\chi_i, \boldsymbol{\theta}, t_i). \tag{16}$$

The design of the control law $g(\cdot)$ will be discussed in Section 2.2.1. To guarantee the operation of the actuators in a safe interval of control actions, an upper limit a_{pmax} and a lower limit a_{pmin} need to be established, yielding

$$a_{pmin} \leq a_p(t_i) \leq a_{pmax}. \tag{17}$$

The safe interval is chosen between $a_{pmax} \leq 60$ and $a_{pmin} \geq -60$, because these values correspond to 60% of the maximum rotational speed of the propellers. In addition, the continuous dynamics (1)–(3), (7)–(10) are discretised using Euler's method leading to

$$\chi_{i+1} = \chi_i + \Delta T \cdot f(\chi_i, a_p(t_i)). \tag{18}$$

As mentioned above, the objective is to minimise the integral square error of the vehicle's trajectory and energy consumed to reach a region around the target point. This suggest the cost function be expressed as

$$J_{Tot}(\boldsymbol{\theta}, \chi_{\mathbf{0}}) = (1 - \lambda) \cdot J_{ISE}(\boldsymbol{\theta}, \chi_{\mathbf{0}}) + \lambda \cdot J_E(\boldsymbol{\theta}, \chi_{\mathbf{0}}), \tag{19}$$

where J_{ISE} and J_E are the discretisation of the Integral Square Error (ISE) between the AUV position and the recovery point for a given trajectory and the discretisation of the energy consumption of the vehicle, respectively, where $0 < \lambda < 1$ is a weighting factor. The term J_{ISE} corresponding to the integral square error of the vehicle's trajectory can be written as

$$J_{ISE}(\boldsymbol{\theta}, \chi_{\mathbf{0}}) = \sum_{i=0}^{n} \left((x_r - x_i)^2 + (y_r - y_i)^2 \right) \cdot \Delta T, \tag{20}$$

where x_i and y_i are the vehicle coordinates at time t_i obtained recursively applying Eq. (18) as a function of the control law a_p, x_r and y_r are the coordinates of the recovery point, and the final number of samples is $n = T_f / \Delta T$. The term J_E corresponding to the energy consumption is defined as

$$J_E(\boldsymbol{\theta}, \chi_{\mathbf{0}}) = \sum_{i=0}^{n} P(u_i, r_i, a_p(t_i), t_i) \cdot \Delta T, \tag{21}$$

where $P(u_i, r_i, a_p(t_i), t_i)$ is the instantaneous electrical power consumption, as explained in Section 2.2.2.

The vehicle must be able to reach the target point from any initial condition. Thus, the objective is to determine, by solving a min–max problem, the parameters $\boldsymbol{\theta}^*$ that minimise the cost function (19) for the worst case in the domain of initial conditions, that is,

$$\boldsymbol{\theta}^* = \arg\min_{\boldsymbol{\theta}} \max_{\chi_{\mathbf{0}} \in \Omega} J_{Tot}(\boldsymbol{\theta}, \chi_{\mathbf{0}}) \tag{22}$$

subject to Eqs. (15)–(21).

The optimisation scenario considered is the one in which the vehicle is required to reach the reference point and wait there to be picked up after a fixed time horizon (t_f, T_f). Since the vehicle must wait until it is recovered, it must consume as little instantaneous power as possible to maximise the operating time.

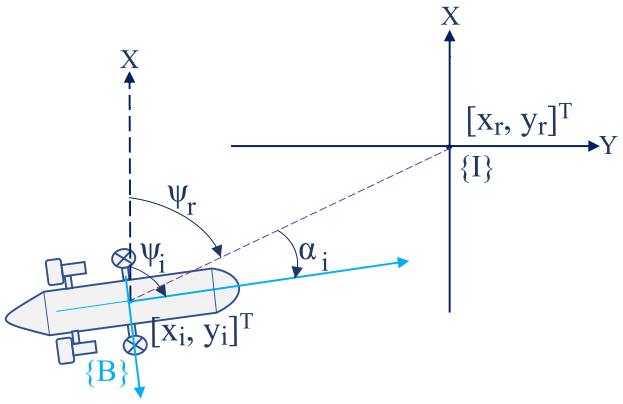

Fig. 3. Variables involved in the control law (23)–(26).

2.2.1. Control law

In Chaos et al. (2022) a discrete fault tolerant control law to drive an AUV with a single thruster was presented and in Cerrada et al. (2023) several alternatives for improving it were explored. Building upon and expanding the set of ideas presented in Cerrada et al. (2023), the control law described next hinges on the computation of the angle between the X-axis of the AUV and the line that connects its centre of mass with the recovery point. In order to compute the control law, first, the angle ψ_r between the vehicle's position $[x_i, y_i]^T$ and the recovery point is calculated as

$$\psi_r = a\tan 2(y_r - y_i, x_r - x_i). \tag{23}$$

Second, the relative angle of the vehicle's orientation with respect to the recovery point at the instant t_i is also computed as (see the notation in Fig. 3)

$$\alpha_i = \psi_i - \psi_r. \tag{24}$$

Notice that the control law is desirable to be invariant under a global rotation of the coordinate frame so that it only depends on the relative angle α.

Since ψ, and $\psi' = \psi + 2m\pi, for\ m \in \mathbb{N}$ should correspond to the same orientation of the vehicle, then α and $\alpha' = \alpha + 2m\pi$ must produce the same control action, thus the control action is a periodic function of α.

For the above reasons and to obtain a continuous and smooth control law, an universal approximant for periodic signals, in the form of a Fourier Series, is used to parameterise the control law of the form

$$h(\alpha_i, \boldsymbol{\theta}) = \frac{b_0}{2} + \sum_{j=1}^{N}(b_j \cdot \cos(j \cdot \alpha_i) + c_j \cdot \sin(j \cdot \alpha_i)). \tag{25}$$

The use of the Fourier series is justified by the intrinsic periodicity of the control signals, i.e., a full rotation of the vehicle produces a change of $\pm 2\pi$ on α. The Fourier series is composed by a sum of cosines and sines (Tolstov & Silverman, 1976) as shown in Eq. (25), where N is the order of the series, and $\boldsymbol{\theta} = [b_0; b_j; c_j],\ \forall j \in [1, N]$ are coefficients that will play the role of optimisation variables in what follows.

Finally, the control action $a_p(t_i)$ is saturated to ensure that its value lies between the maximum and minimum values that are physically possible, that is,

$$a_p(t_i) = g(\alpha_i, \boldsymbol{\theta}, t_i) = \min(a_{pmax}, \max(a_{pmin}, h(\alpha_i, \boldsymbol{\theta}))). \tag{26}$$

It is important to remark that although this paper deals with a_p, the control law is valid for both horizontal thrusters, i.e., if the failed thruster were the portside one, the control action a_s would be also computed using Eq. (26) by simply replacing $h(\alpha_i)$ with $h(-\alpha_i)$. Note that, due to the symmetry of the vehicle, the failed portside thruster is a reflection of the failed starboard one and this does not affect the dynamics of the vehicle, but only the sign of the angles involved.

As a summary, the flow chart of the proposed control law scheme is illustrated in Fig. 4.

2.2.2. Model of energy consumed by the thrusters

A model of the instantaneous electrical power consumed by the thrusters is described in Häusler (2015) for the MEDUSA class vehicles. In the scenario at hand the vehicle only has the portside thruster in operational conditions, thus the model in Häusler (2015) is reduced to

$$P(u_i, r_i, a_p(t_i), t_i) = \mathcal{R}_a \cdot I_p(u_i, r_i, a_p(t_i)) + K_e \cdot n_p(a_p(t_i)) + P_p, \tag{27}$$

where $I_p(u_i, r_i, a_p(t_i))$ is the intensity of the electric current required to move the portside thruster, $\mathcal{R}_a$ is the thruster's electric resistance, K_e its electrical constant, $n_p(a_p(t_i))$ denote rotational velocity of the thruster, and P_p is the constant power required by the on-board computers and other hotel payload.

Following the low-order harmonic approximation of a Four-Quadrant Propeller Model, named the L-model in Häusler (2015), the current I_p is computed as

$$I_p = (b \cdot w_p + Q_p)/K_t \tag{28}$$

where b is propeller's viscous friction coefficient, K_t is the torque constant, w_p is the propeller rotational velocity in rad/s (see Eqs. (4)–(5)), and Q_p is the propeller torque.

The variable Q_p is in turn defined as

$$Q_p = \rho/2 \cdot C_Q \cdot (\mathrm{v}_{a_p}^2 + \mathrm{v}_{p_p}^2) \cdot \pi \cdot R_p^2 \cdot d_p \tag{29}$$

where ρ is the seawater density, R_p and d_p are the radius and the diameter of the propeller, respectively, v_{a_p} is propeller's advance velocity, defined as $\mathrm{v}_{a_p} = u - l_y \cdot r$, where l_y is the y component of the distance from the centre of the propeller to the centre of mass of the vehicle in the body frame, v_{p_p} is the lateral velocity of the propeller blade at a radius of $k_1 \cdot R_p$, expressed as $\mathrm{v}_{p_p} = k_1 \cdot R_p \cdot w_p$, where k_1 is a constant that describes the interaction of the propeller blade with the water in the L-model, and C_Q is the coefficient defined in terms of the advance angle of the propeller $\beta_p = a\tan 2(\mathrm{v}_{a_p}, \mathrm{v}_{p_p})$ according to

$$C_Q = (-k_1/2) \cdot (-C_L^L \cdot \sin(\beta_p) - C_D^L \cdot \cos(\beta_p)), \tag{30}$$

$$C_L^L = C_L^{max} \cdot \sin(2 \cdot (\gamma_p - o_L)), \tag{31}$$

$$C_D^L = (C_D^{max} - C_D^{min}) \cdot (1 - \cos(2 \cdot (\gamma_p - o_D)))/2 + C_D^{min}, \tag{32}$$

$$\gamma_p = \zeta_p - \beta_p, \tag{33}$$

$$\zeta_p = a\tan(k_2/\pi), \tag{34}$$

where k_2, C_L^L, C_D^L, C_L^{max}, C_D^{max}, C_D^{min}, o_L and o_D are the parameters determined in Häusler (2015) for the L-model, γ_p is the angle of attack at the propeller blade, and ζ_p is the pitch angle of the propeller.

2.2.3. Reference control law

For comparison purposes, the control law presented in Chaos et al. (2022) is introduced. It was designed so that the AUV could be driven using a single thruster to a desired safety point, starting from any initial condition. Mathematically, the control law is defined by the following equations,

$$\psi_r = a\tan 2(y_r - y_i, x_r - x_i), \tag{35}$$

$$a_p(t_i) = a_0 + \Delta a \cdot sign(\sin(\psi_i + \Delta\psi - \psi_r)), \tag{36}$$

where $a_p(t_i)$ is the portside thruster control signal as a dimensionless reference for the corresponding angular velocity, $[x_i, y_i]^T$ is the vehicle's position, a_0 is a constant term in the control signal, $\Delta a > 0$ is the magnitude of the change of the control signal with respect to a_0 and $\Delta\psi$ is a correction term that is applied to the angle so that the vehicle goes as straight as possible to its destination. The values of Δa and a_0 are chosen so that the output $a_p(t_i)$ is always positive.

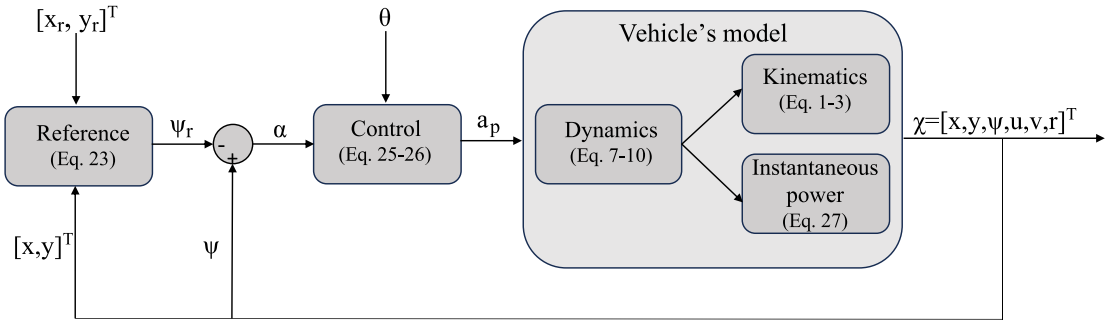

Fig. 4. Flow chart of control law (23)–(26) and vehicle's model.

This control law is used as reference to compare and evaluate the results obtained with the newly proposed control law (23)–(26). An improvement factor (IF) is computed for the different cost functions involved, defined as

$$IF_{Tot,ISE,E}(\%) = \frac{J_{Tot,ISE,E(ref)} - J_{Tot,ISE,E}}{J_{Tot,ISE,E(ref)}} \cdot 100\%, \tag{37}$$

where $J_{Tot,ISE,E(ref)}$ are the values of the cost functions defined in (19)–(21), respectively, for the reference control law shown in (35)–(36) and $J_{Tot,ISE,E}$ are the optimal values of the cost functions obtained in this work for the control law (23)–(26). In order to facilitate the interpretation of the results, they are presented in standardised form as

$$J_{Tot,ISE,E(std)} = \frac{J_{Tot,ISE,E}}{J_{Tot,ISE,E(ref)}}. \tag{38}$$

3. Demonstration of stability and convergence

The existence of a set of parameters θ and constants that satisfy restrictions (15)–(21) must be shown, in order to demonstrate the feasibility of a solution to the optimisation problem (22).

Constraints (16) and (18) are trivially satisfied by solving (1)–(3), (7)–(10) with the Euler method. Constraint (17) is satisfied by the proposed control law since the control action is saturated as shown in Eq. (26), and (19)–(21) are simply recursive formulae for computing the cost function. The only non trivial restriction that remains is (15). Therefore, the proof of stability and convergence focuses on finding a set of parameters θ that satisfies this constraint.

From a practical standpoint, in what follows a numerical solution to the optimisation problem with the cost function introduced in (19) is desired. At this point, however, it is important to show that the type of control law proposed in (25) is indeed suitable for the problem at hand. For this reason, first, the existence of a analytical Globally Ultimately Bounded (GUB) solution in the form (23)–(26) that satisfies (15) will be shown, using rigorous mathematical arguments. This theoretical result legitimises the use of a numerical solution to the optimisation problem with monotonic behaviour (for example GA with elitism) with a view to finding a solution that will converge to a control law satisfying (15), thus guaranteeing that the trajectory of the system will converge to a neighbourhood of the desired point in time t_f and will remain there at least until time T_f. Moreover, as $\Delta T \to 0$ the solution of the discrete problem (22) approaches the solution of the continuous dynamics (1)–(3), (7)–(10) under the control law (23)–(26). Thus, the analysis can be done over the continuous solution of Eqs. (1)–(3), (7)–(10) under control law (23)–(26).

Theorem 1. *There exist parameters of controller (23)–(26) that make the system (1)–(3), (7)–(10) globally ultimately bounded (GUB), that is,*

$$(x(t) - x_r)^2 + (y(t) - y_r)^2 < R_f^2 \quad for \quad t_f \le t \le T_f$$

for some positive constants R_f, t_f and T_f, where T_f is the final recovery time, t_f is the setting time that depends on the initial condition and R_f is a final bound that is independent of the initial condition but bounded below by the minimum turning radius of the vehicle.

Proof. In Chaos et al. (2022), the following statements for system (1)–(3), (7)–(10) were proven:

- Under the control law (35)–(36) the system trajectories converge from any initial condition to a neighbourhood of the reference point $[x_r, y_r]^T$ of radius R_1, i.e.,

$$R(t)^2 = (x(t) - x_r)^2 + (y(t) - y_r)^2 < R_1^2 \quad for \quad t_1 \le t \tag{39}$$

  where t_1 is the setting time for the controller (35)–(36) when the initial condition of the vehicle lies in the bounded region Ω.
- After some transient time, and when a bounded control action is applied ($0 < a_{pmin} \le a_p \le a_{pmax}$) the velocities of the vehicle are bounded by $|u|, |v| \le V_{max}$. In addition the yaw rate is bounded away from zero, that is, $0 < r_{min} \le r \le r_{max}$;
- The control law is GUB with $\Delta a = \frac{a_{pmax} - a_{pmin}}{2}$ arbitrary small.

For the sake of clarity, in the following, the reference control law (36) is defined as $a_{p_{ref}}$ and the Fourier series control law (26) as $a_{p_{FS}}$. Now, first note that (36) can be written as

$$a_{p_{ref}}(\chi(t), t) = a_0 + \Delta a \cdot sign(\sin(\alpha + \Delta\psi))$$

where $\alpha = \psi - \psi_r$. On the other hand, from (26) consider that

$$a_{p_{FS}}(\chi(t), t) = \min(a_{pmax}, \max(a_{pmin}, h(\alpha, \theta))) \tag{40}$$

where $h(\alpha, \theta) = \kappa \cdot \sin(\alpha + \Delta\psi)$, with κ being a positive constant. By using the angle sum trigonometric identity $\sin(\alpha + \Delta\psi) = \cos(\Delta\psi) \cdot \sin(\alpha) + \sin(\Delta\psi) \cdot \cos(\alpha)$, it follows that

$$h(\alpha, \theta) = \kappa \cdot \cos(\Delta\psi) \cdot \sin(\alpha) + \kappa \cdot \sin(\Delta\psi) \cdot \cos(\alpha) = \\ = c_1 \cdot \sin(\alpha) + b_1 \cdot \cos(\alpha).$$

Notice that the above is in the form of the proposed control law (23)–(26) for $N = 1$ and $b_0 = 0$. Moreover, if a_0 and Δa are chosen so as a_{pmin} is always positive, then $a_{pmax} = a_0 + \Delta a > a_{pmin} > 0$, and $a_{p_{ref}}$ and $a_{p_{FS}}$ are equal unless

$$\frac{a_{pmin}}{\kappa} < \sin(\alpha + \Delta\psi) < \frac{a_{pmax}}{\kappa}. \tag{41}$$

In this case,

$$|a_{p_{ref}} - a_{p_{FS}}| < a_{pmax} - a_{pmin} = 2\Delta a. \tag{42}$$

To verify this, notice that Eq. (40) is just a saturation of $h(\alpha, \theta)$, given by

$$a_{p_{FS}} = \begin{cases} a_{pmin} & if \quad h(\alpha, \theta) < a_{pmin} \\ a_{pmax} & if \quad h(\alpha, \theta) > a_{pmax} \\ h(\alpha, \theta) & otherwise \end{cases}$$

Then, if $\sin(\alpha + \Delta\psi) > \frac{a_{pmax}}{\kappa} > 0$, it follows that $h(\alpha, \theta) > a_{pmax}$ and therefore $a_{p_{FS}} = a_{p_{ref}} = a_{pmax}$. Moreover, if $\sin(\alpha + \Delta\psi) < \frac{a_{pmin}}{\kappa}$

then $h(\alpha,\theta) < a_{pmin}$ and therefore $a_{p_{FS}} = a_{p_{ref}} = a_{pmin}$. Furthermore, if none of these conditions hold, $a_{p_{ref}}$ and $a_{p_{FS}}$ are both in the range (a_{pmin}, a_{pmax}), and (42) always holds.

Consider now the solutions $\chi(t)$ and $\chi'(t)$ of system (1)–(3), (7)–(10) under control laws $a_{p_{ref}}$ and $a_{p_{FS}}$, respectively, starting at the same initial condition χ_0. In general, variables obtained from $a_{p_{FS}}$ are denoted with " $'$ " and variables from $a_{p_{ref}}$ without it. Consider also (39) and let t_f be the time that the vehicle will take to reach the neighbourhood of the reference point $(x(t)-x_r)^2 + (y(t)-y_r)^2 < R_1^2, \quad for \quad t_f \le t$.

The aim is to demonstrate that the trajectory will reach the circumference of radius R_2 centred at the reference point X_r in at least t_f seconds, where

$$R_2 = \max\left(R_1 + \epsilon_1, \frac{4V_{max}}{r_{min}}\right)$$

and ϵ_1 is a positive constant that can be made as small as desired.

First note that if $R(t) \le R_{min} = \frac{4V_{max}}{r_{min}}$ then vehicle is already inside a circle of radius $R_{min} < R_2$ as desired, otherwise the derivative of both α and α' are bounded away from zero if $R(t) > R_{min}$ since

$$\dot\alpha = \dot\psi - \dot\psi_r = r - \frac{\dot y(t)\cdot(x(t)-x_r) - \dot x(t)\cdot(y(t)-y_r)}{(x(t)-x_r)^2 + (y(t)-y_r)^2}. \tag{43}$$

Notice that $0 < r_{min} < r$ (the vehicle is always turning clockwise) and the second term of (43) can be bounded by

$$\left|\frac{\dot y(t)\cdot(x(t)-x_r) - \dot x(t)\cdot(y(t)-y_r)}{(x(t)-x_r)^2 + (y(t)-y_r)^2}\right| \le \le \frac{V_{max}\cdot R(t) + V_{max}\cdot R(t)}{R(t)^2} = \frac{2V_{max}}{R(t)}.$$

In this case, $R(t) > R_{min} = \frac{4V_{max}}{r_{min}}$, and thus

$$\dot\alpha > r_{min} - \frac{2V_{max}}{R_{min}} > r_{min} - \frac{r_{min}}{2} = \frac{r_{min}}{2}.$$

Furthermore, the partial derivatives of α with respect to the state are bounded as

$$\left|\frac{\partial\alpha}{\partial x}\right| = \left|\frac{-y}{x^2+y^2}\right| \le \frac{1}{R(t)}, \left|\frac{\partial\alpha}{\partial y}\right| = \left|\frac{x}{x^2+y^2}\right| \le \frac{1}{R(t)} \ and \ \frac{\partial\alpha}{\partial\psi} = 1.$$

Thus,

$$\left\|\frac{\partial\alpha}{\partial\chi(t)}\right\| \le \sqrt{\frac{2+R_2^2}{R_2^2}} = \delta_1 \rightarrow \tag{44}$$
$$\rightarrow |\alpha(\chi(t)) - \alpha(\chi'(t))| \le \delta_1 \|\chi(t) - \chi'(t)\|.$$

In order to study the difference between the reference controller $a_{p_{ref}}$ and the proposed one $a_{p_{FS}}$, consider a partition of the time interval (t_0, t_f) into slices $[t_i, t_{i+1}]$ such that there is at most one revolution in each time interval, i.e.

$$\Delta t = t_{i+1} - t_i < \frac{2\pi}{r_{max}}. \tag{45}$$

Then, the solutions of (1)–(10) in this time interval are given in terms of solutions to the differential equations

$$\dot\chi(t) = f(\chi(t), a_{p_{ref}}(\chi(t),t)); \quad \chi_0 = \chi(t_i),$$

and

$$\dot\chi'(t) = f(\chi'(t), a_{p_{FS}}(\chi'(t),t)); \quad \chi'_0 = \chi'(t_i),$$

from which it follows that

$$\chi(t) = \chi_0 + \int_{t_i}^{t_{i+1}} f(\chi(s), a_{p_{ref}}(\chi(s),s))\, ds, \tag{46}$$

$$\chi'(t) = \chi'_0 + \int_{t_i}^{t_{i+1}} f(\chi'(s), a_{p_{FS}}(\chi'(s),s))\, ds. \tag{47}$$

Subtracting (46) and (47) and taking norms yields

$$e(t) = \|\chi(t) - \chi'(t)\| \le \int_{t_i}^{t_{i+1}} \| f(\chi(s), a_{p_{ref}}(\chi(s),s)) - - f(\chi'(s), a_{p_{FS}}(\chi'(s),s)) \|\ ds + e(t_i),$$

where $e(t_i)$ is the error calculated at time t_i.

Note that f is Lipschitz with respect to the first argument with Lipschitz constant L_c since the velocities are bounded, but $a_{p_{ref}}$ is discontinuous at the switching points $\alpha + \Delta\psi = m\pi, for\ m \in \mathbb{N}$, and $a_{p_{FS}} \to a_{p_{ref}}$ as $\kappa \to \infty$. In what follows, for simplicity of exposition and with an abuse of notation, $\chi(s)$ and $\chi'(s)$ are henceforth written as χ and χ' leading to

$$\|f(\chi, a_{p_{ref}}(\chi)) - f(\chi', a_{p_{FS}}(\chi'))\| = \|f(\chi, a_{p_{ref}}(\chi)) - - f(\chi', a_{p_{ref}}(\chi)) + f(\chi', a_{p_{ref}}(\chi)) - f(\chi', a_{p_{FS}}(\chi'))\| \le \le \|f(\chi, a_{p_{ref}}(\chi)) - f(\chi', a_{p_{ref}}(\chi))\| + \| f(\chi', a_{p_{ref}}(\chi)) - - f(\chi', a_{p_{FS}}(\chi'))\|.$$

Now, solving (1)–(10) for $\dot\chi$ and taking the difference, yields

$$f(\chi', a_{p_{ref}}(\chi)) - f(\chi', a_{p_{FS}}(\chi')) = \begin{bmatrix} 0 \\ 0 \\ 0 \\ \frac{F_p(a_{p_{ref}}) - F_p(a_{p_{FS}})}{m_u} \\ 0 \\ \frac{L\cdot F_p(a_{p_{ref}}) - L\cdot F_p(a_{p_{FS}})}{m_r} \end{bmatrix} = = \left[0,\ 0,\ 0,\ \frac{K}{m_u},\ 0,\ \frac{LK}{m_r}\right]^T \cdot (|a_{p_{ref}}|\cdot a_{p_{ref}} - |a_{p_{FS}}|\cdot a_{p_{FS}}).$$

Thus,

$$\|f(\chi, a_{p_{ref}}(\chi)) - f(\chi', a_{p_{FS}}(\chi'))\| \le L_c\cdot\|\chi - \chi'\| + + \left\|\left[0\ 0\ 0\ \frac{K}{m_u}\ 0\ \frac{LK}{m_r}\right]^T\right\| \cdot \left||a_{p_{ref}}|\cdot a_{p_{ref}} - |a_{p_{FS}}|\cdot a_{p_{FS}}\right| \le \le L_c e(t) + \delta_2\cdot|a^2_{p_{ref}}(\chi) - a^2_{p_{FS}}(\chi')|$$

where $\delta_2 = \left\|\left[0\ 0\ 0\ \frac{K}{m_u}\ 0\ \frac{LK}{m_r}\right]^T\right\|$. It follows from (46) that

$$e(t) \le L_c\Delta t \sup_{t\in[t_i,t_{i+1}]} e(t) + \int_{t_i}^{t_{i+1}} \delta_2\cdot|a^2_{p_{ref}}(\chi) - a^2_{p_{FS}}(\chi')|\ ds + + e(t_i).$$

Notice now that

$$\int_{t_i}^{t_{i+1}} \delta_2\cdot|a^2_{p_{ref}}(\chi) - a^2_{p_{FS}}(\chi')|ds = = \int_{t_i}^{t_{i+1}} \delta_2\cdot|a^2_{p_{ref}}(\chi) - a^2_{p_{ref}}(\chi') + a^2_{p_{ref}}(\chi') - a^2_{p_{FS}}(\chi')|ds \le \le \int_{t_i}^{t_{i+1}} \delta_2\cdot|a^2_{p_{ref}}(\chi) - a^2_{p_{ref}}(\chi')|ds + + \int_{t_i}^{t_{i+1}} \delta_2\cdot|a^2_{p_{ref}}(\chi') - a^2_{p_{FS}}(\chi')|ds.$$

The integrand $|a^2_{p_{ref}}(\chi') - a^2_{p_{FS}}(\chi')|$ is zero unless condition (41) holds, which is equivalent to $m\pi - \arcsin\left(\frac{a_{pmin}}{\kappa}\right) < \alpha' + \Delta\psi < m\pi + \arcsin\left(\frac{a_{pmax}}{\kappa}\right)$ and can otherwise be bounded by $|a^2_{pmax} - a^2_{pmin}|$.

Since α' is strictly increasing at least at the rate $\frac{r_{min}}{2}$, this condition can only hold for at most a time $dt_1 = \frac{2}{r_{min}}\left(\arcsin\left(\frac{a_{pmax}}{\kappa}\right) + \arcsin\left(\frac{a_{pmin}}{\kappa}\right)\right) < \frac{4}{r_{min}}\arcsin\left(\frac{a_{pmax}}{\kappa}\right)$, so that the integral of $|a^2_{pmax} - a^2_{pmin}|$ during this time interval can be bounded by $|a^2_{pmax} - a^2_{pmin}|\cdot dt_1$. In addition, this can only happen two times per revolution (when $\alpha' = 2m\pi$ and $\alpha' = (2m+1)\pi$). Therefore,

$$\int_{t_i}^{t_i+1} \delta_2\cdot|a^2_{p_{ref}}(\chi') - a^2_{p_{FS}}(\chi')|ds \le 2\delta_2|a^2_{pmax} - a^2_{pmin}|dt_1 \le$$

$$\leq \delta_3 \cdot \arcsin\left(\frac{a_{pmax}}{\kappa}\right) = \epsilon_2,$$

where $\delta_3 = \frac{8\delta_2(a_{pmax}^2 - a_{pmin}^2)}{r_{min}}$. Note that ϵ_2 can be made as small as needed by making $\kappa \to \infty$.

For the other term $|a_{p_{ref}}^2(\chi) - a_{p_{ref}}^2(\chi')| = |a_{p_{ref}}^2(\alpha) - a_{p_{ref}}^2(\alpha')|$, $a_{p_{ref}}$ can only take values a_{pmax} and a_{pmin}. To be different from zero one of the control actions must be a_{pmax} and the other a_{pmin} and this condition can only be maintained until one of the two control actions switches.

Now suppose first that at some time t^* the control action $a_{p_{ref}}(\chi)$ switches to a_{pmax} while $a_{p_{ref}}(\chi') = a_{pmin}$. Then, $\alpha(t^*) = 2m'\pi - \Delta\psi$ and $(2m-1)\pi - \Delta\psi < \alpha'(t^*) < 2m\pi - \Delta\psi$ for some integers m' and m.

If $m = m'$, then $(2m'-1)\pi - \Delta\psi < \alpha' < \alpha = 2m'\pi - \Delta\psi$, and since $\alpha'(t)$ is strictly increasing at least at rate $\frac{r_{min}}{2}$, it becomes $\alpha(t^*)$ in at least time $dt_2 = \frac{2|\alpha(t^*) - \alpha'(t^*)|}{r_{min}}$. Considering now the bound (44), dt_2 can be bounded as $dt_2 \leq \frac{2\delta_1\|\chi(t^*) - \chi'(t^*)\|}{r_{min}} = \frac{2\delta_1 e(t^*)}{r_{min}}$. Otherwise the control action will switch even earlier, because in this case $\pi < |\alpha(t^*) - \alpha'(t^*)|$ and the angle to the next switch is always less than π.

The other switches are similar, and as these transitions can happen two times per revolution this yields

$$\int_{t_i}^{t_{i+1}} |a_{p_{ref}}^2(\chi) - a_{p_{ref}}^2(\chi')| \leq 4|a_{pmax}^2 - a_{pmin}^2| dt_2 \leq$$
$$\leq \frac{4\delta_1|a_{pmax}^2 - a_{pmin}^2|}{r_{min}} \sup_{t\in[t_i,t_{i+1}]} e(t).$$

Thus,

$$e(t) \leq \left(L_c\Delta t + \frac{4\delta_2\delta_1(a_{pmax}^2 - a_{pmin}^2)}{r_{min}}\right) \sup_{t\in[t_i,t_{i+1}]} e(t) + \epsilon_2 + e(t_i). \tag{48}$$

But now choose $\Delta t < \min(\frac{1}{4L_c}, \frac{4\pi}{r_{max}})$, so that condition (45) is satisfied and $L_c\Delta t \leq \frac{1}{4}$, and $\frac{4\delta_2\delta_1(a_{pmax}^2 - a_{pmin}^2)}{r_{min}} \leq \frac{1}{4}$ (the latter always holds by making the interval (a_{pmax}, a_{pmin}) small enough) and take the supremum on the left hand side of (48) to successively obtain

$$\sup_{t\in[t_i,t_{i+1}]} e(t) \leq \left(\frac{1}{4} + \frac{1}{4}\right) \sup_{t\in[t_i,t_{i+1}]} e(t) + e(t_i) + \epsilon_2,$$
$$\frac{1}{2} \sup_{t\in[t_i,t_{i+1}]} e(t) \leq e(t_i) + \epsilon_2,$$
$$\sup_{t\in[t_i,t_{i+1}]} e(t) \leq 2e(t_i) + 2\epsilon_2.$$

In particular, for times t_i and t_{i+1} the following recurrence relation for the error holds

$$e(t_{i+1}) \leq 2e(t_i) + 2\epsilon_2.$$

Since both control laws start from the same initial condition $e(t_0) = 0$,

$$e(t_1) \leq 2e(t_0) + 2\epsilon_2 = 2\epsilon_2,$$
$$e(t_2) \leq 2e(t_1) + 2\epsilon_2 = 4\epsilon_2 + 2\epsilon_2,$$
$$\ldots$$
$$e(t_n) \leq (2^n + 2^{n-1} \ldots + 2)\epsilon_2 = (2^{n+1} - 2)\epsilon_2 \leq$$
$$\leq \left(2^{\left[\frac{t_f - t_0}{\Delta t}\right]+1} - 2\right)\epsilon_2 = \epsilon_1,$$

where ϵ_1 can be made arbitrary small as $\kappa \to \infty$, and thus $e(t)$ can be made arbitrary small during the time interval (t_0, t_f) by choosing κ high enough.

To finish the proof note that for $t > t_f$, when the controller $a_{p_{ref}}$ is applied, the vehicle lies in a circumference of radius R_1, and since the trajectories for both controllers are separated by less than ϵ_1, the trajectory of the vehicle will eventually (at least at time t_f) reach the circumference of radius $R_1 + \epsilon_1 \leq R_2$. Once there, the vehicle could go again outside the circumference, but as soon as the vehicle leaves the circle the same argument applies again with a $t_f' < t_f$. Therefore, the furthest that the vehicle can go away from the centre of the circumference is $R_2 + V_{max} \cdot t_f'$ so that

$$(x(t) - x_r)^2 + (y(t) - y_r)^2 \leq (R_2 + V_{max} \cdot t_f')^2 = R_f^2 \quad for \quad t_f \leq t,$$

which concludes the proof.

4. Results

This section is organised as follows: Section 4.1 describes the implementation and set up used to solve the optimisation problem defined in Section 2.2, Section 4.2 focuses on the optimisation results, Section 4.3 compares the optimisation results with a MPC scheme and in Section 4.4 the resultant optimal control law is tested on the simulator of the Dynamical System and Ocean Robotics group of the Institute for Systems and Robotics (DSOR-ISR) of the Instituto Superior Tecnico, University of Lisbon.

4.1. Implementation and set up

In order to solve the min–max optimisation problem (22) and to show convergence of the vehicle's trajectory to a neighbourhood of the desired recovery area (15) from any initial condition, different initial conditions for the vehicle are generated using a Monte Carlo method (Kroese et al., 2014).

The method works as follows. First, the inner maximisation problem of (22) consists in finding the maximum cost for any initial condition in the set Ω, computed as

$$J_{max}(\boldsymbol{\theta}) = \max_{\chi_0\in\Omega} J_{Tot}(\boldsymbol{\theta}, \chi_0).$$

In order to do so, a set of 100 initial conditions are sampled randomly from Ω, for each of them the cost J_{Tot} is evaluated and the biggest one is chosen as $J_{max}(\boldsymbol{\theta})$.

Notice that the sampling process can be enhanced by taking into account the invariance of the control law and the set Ω under a rotation of the coordinate frame, thus without loss of generality, χ_0 can be sampled as

$$\chi_0 = [100 \cdot rand_1,\ 0,\ 2\pi \cdot rand_2,\ 0,\ 0,\ 0]^T$$

where $rand_1$ and $rand_2$ are two uniform random numbers in the interval [0 1].

Once the inner maximisation has been solved, the second part of the method begins, which is the outer minimisation problem formulated as

$$\boldsymbol{\theta}^* = \arg\min_{\boldsymbol{\theta}} J_{max}(\boldsymbol{\theta}).$$

The above is solved iteratively using a GA until the stop condition is reached.

In order to compute the coefficients $\boldsymbol{\theta}$ of the Fourier series that define the optimal control law, the solution obtained in Cerrada et al. (2023) is used as the initial seed. This seed is used for each value of the weighting factor λ. Subsequent optimisations for each value of λ consider the previous optimal value of $\boldsymbol{\theta}$ as the initial seed. The process was repeated until no further improvement of the coefficients was achieved, and this final coefficients are presented in Appendix B, Table B.8.

The weighting factor has been set from $\lambda = 0.05$ to $\lambda = 0.95$ with increments of $\Delta\lambda = 0.05$. Note that $\lambda = 0$ corresponds to the case in which the vehicle must reach the target point as soon as possible, so that energy consumption is not taken into account, and $\lambda = 1$ means that the vehicle remains stationary to avoid energy consumption.

The worst initial condition used corresponds to a distance to the target of 99.36 metres and a relative orientation to the target of 45 degrees for the case of $\lambda = 0.05$, that is,

$$\chi_{0_w} = [70.26\,\text{m},\ 70.26\,\text{m},\ 5.14\,\text{rad},\ 0\ \text{m/s},\ 0\ \text{m/s},\ 0\,\text{rad/s}]^T,$$

The recovery point is defined as the centre of the inertial coordinate frame, and the rest of the parameters selected to implement the problem are found in Table 2.

Table 2
Simulations set up.

Category	Parameters values
Vehicle's model	$X_u = -0.2\ \text{kg} \cdot \text{s}^{-1}$
	$X_{\|u\|} = -25\ \text{kg} \cdot \text{m}^{-1}$
	$Y_v = -55.1\ \text{kg} \cdot \text{s}^{-1}$
	$Y_{\|v\|} = -101.3\ \text{kg} \cdot \text{m}^{-1}$
	$N_r = -4.14\ \text{kg} \cdot \text{m}^2 \cdot \text{s}^{-1}$
	$N_{\|r\|} = -6.23\ \text{kg} \cdot \text{m}^2$
	$K = 3.6 \cdot 10^{-3}$ N
	$L = 0.25$ m
	$m_u = 37$ kg
	$m_v = 47$ kg
	$m_r = 4.64\ \text{kg} \cdot \text{m}^2$
Genetic algorithm	tolerance value $= 10^{-4}$
	population size $= 200$
	max. num. generations $= 10^3$
Time	$\Delta T = 0.1$ s
	$T_f = 1600$ s
Reference control law	$a_0 = 45$
	$\Delta a = 15$
	$\Delta\psi = -63°$
	$J_{ISE(ref)} = 5.1006 \cdot 10^6\ \text{m}^2 \cdot \text{s}$[a]
	$J_{E(ref)} = 5.3712 \cdot 10^4$ J[a]
Energy consumption model[b]	$\mathcal{R}_a = 0.66\ \Omega$
	$K_e = K_t = 0.259022\ \text{N} \cdot \text{m/A}$
	$P_p = 26$ W
	$b = 10^{-6}\ \text{N} \cdot \text{m} \cdot \text{s}$
	$n_{max} = 71.6\ \text{s}^{-1}$
	$\rho = 1023.0\ \text{Kg/m}^3$
	$d_p = 2 \cdot R_p = 0.076$ m
	$l_y = 0.15$ m
	$k_1 = 0.7$
	$C_L^{max} = 0.5749$
	$C_D^{max} = 1.0383$
	$C_D^{min} = 0.0273$
	$o_L = -1.6157°$
	$o_D = 1.9309°$
	$k_2 = 1.35$

[a] Obtained from $\chi_{\mathbf{0}_w}$.

[b] These values are defined in Häusler (2015) for a MEDUSA class vehicle.

Table 3
Standardised cost functions and improvement factors for different weighting factors.

λ	$J_{ISE(std)}$	$J_{E(std)}$	$J_{Tot(std)}$	IF_{ISE}	IF_E	IF_{Tot}
0.05	0.741	0.908	0.750	25.88	9.24	25.04
0.20	0.743	0.891	0.772	25.74	10.91	22.78
0.35	0.746	0.874	0.791	25.45	12.56	20.94
0.50	0.754	0.860	0.807	24.59	14.03	19.31
0.65	0.764	0.850	0.820	23.57	15.00	18.00
0.80	0.803	0.835	0.829	19.69	16.46	17.10
0.95	0.867	0.824	0.826	13.28	17.57	17.35

4.2. Optimisation results

Fig. 5(a) depicts the Pareto front of the cost function of standardised integral squared error versus standardised energy consumption. It can be seen that increasing the weighting factor from 0.05 to 0.7 produces a more significant improvement in energy savings than the worsening of the ISE. However, from $\lambda = 0.7$ to $\lambda = 0.95$, there is a significant degradation of the ISE. In Fig. 5(b) it is shown the integral squared error (ISE), energy (E) and total (Tot) improvement factor (IF) for each weighting factor. It is clear that a sharp change for the ISE occurs at $\lambda = 0.70$, which means that the trajectory can deviate significantly from the target point and take longer to reach it. Notice how the increase in the energy improvement and the decrease of total improvement are progressive and smooth. (See Table 3.)

The control actions, obtained from control law (23)–(26) and coefficients θ of Table B.8, for different weighting factors are shown in Fig. 6 with respect to the relative orientation angle α of the vehicle. It can be seen how as the weighting factor increases, the magnitude of the actions decreases. This means that slow thruster turns and therefore longer journeys of the vehicle are favoured to save energy. In Fig. 7 the control actions with respect to time are represented for different weighting factors. For the sake of clarity, only 3 curves are plotted, which correspond to $\lambda = 0.05$, $\lambda = 0.50$ and $\lambda = 0.95$. Notice that as the weighting factor increases, lower values of the control actions are commanded, their frequency decreases and it takes longer to reach the target point. The maximum delay to reach the destination between the extreme situations analysed is 200 seconds. The initial condition in Figs. 6 and 7 is $\chi_{\mathbf{0}_w}$.

Finally, Fig. 8 illustrates the progress on the X-axis and Y-axis for the vehicle trajectory from $\chi_{\mathbf{0}_w}$ to the recovery point (dark blue dashed line) for $\lambda = 0.05$, $\lambda = 0.50$ and $\lambda = 0.95$. It is observed how for $\lambda = 0.95$, in which the coefficients have been optimised favouring the minimum energy consumption, it takes longer (approximately 200 seconds) to reach the destination point than the case with $\lambda = 0.05$, where the coefficients have been optimised to favour the decrease of the trajectory ISE. The $\lambda = 0.50$ case, where energy and ISE are optimised with the same weight, takes only about 30 seconds more than the $\lambda = 0.05$ case to reach the target.

4.3. Comparison with MPC scheme

In this section, a comparative analysis between the control approach based on Fourier Series explained above and MPC is carried out. The election of MPC for this comparison is because, to the best of the author's knowledge, there are no similar control laws in the literature addressing the same operating conditions, i.e., an AUV whose motion in the horizontal plane is executed by using one single stern thruster, given that the other stern thruster is inoperative. Granted, previous work by some of the co-authors of the present paper published in Chaos et al. (2022), which is the control law used as reference in the next subsection, and Cerrada et al. (2023) addresses the problem of driving an AUV operating with a single thruster to a destination point. However, in striking contrast to the work reported here energy constraints are not taken directly into account.

Then, the aim of the following comparison is to check the behaviour and suitability of the proposed control law against a well-known approach that provides good results for path planning and tracking problems, see for example (Hung et al., 2020; Hung & Pascoal, 2018). Moreover, the reasons because MPC is not considered for comparison in the next subsection are highlighted, making MPC and similar approaches not suitable for the scenario under study.

The MPC scheme is a control technique that forecasts the output of the entire system based on past and future input data. It is based on three principles, i.e., rolling optimisation, feedback correction, and predictive modelling (Gong et al., 2014). The biggest advantage of MPC is that the current time interval is optimised taking into account future time intervals, so the performance of real-time control can be improved (Bashir et al., 2023). This technique has also been used in recent years both to deal with fault-tolerant control (Ding & Zhu, 2020) and to minimise energy consumption (Yao et al., 2019).

The MPC designed for the comparison is run with a sliding time window of 60 seconds, with a sampling time of 1 seconds (the optimal control action is computed for each second). Several sizes for the sliding time window were tested, and the size of 60 seconds selected was the most suitable for the problem at hand in terms of computing time and convergence to the destination point. A horizon less than 60 seconds is not enough for the controller to find a suitable control action and more than 60 seconds makes the calculations very slow.

Considering this setup, every single optimisation has a computation time around 5.2 seconds (in a laptop with processor 11th Gen Intel(R) Core(TM) i7-11800H @ 2.30 GHz and 32 Gb of RAM), which gives us a lower bound to compute and implement the control actions. Moreover, the computer on board the AUV has less performance, so this lower bound will be larger in practice. For this reason, the control horizon

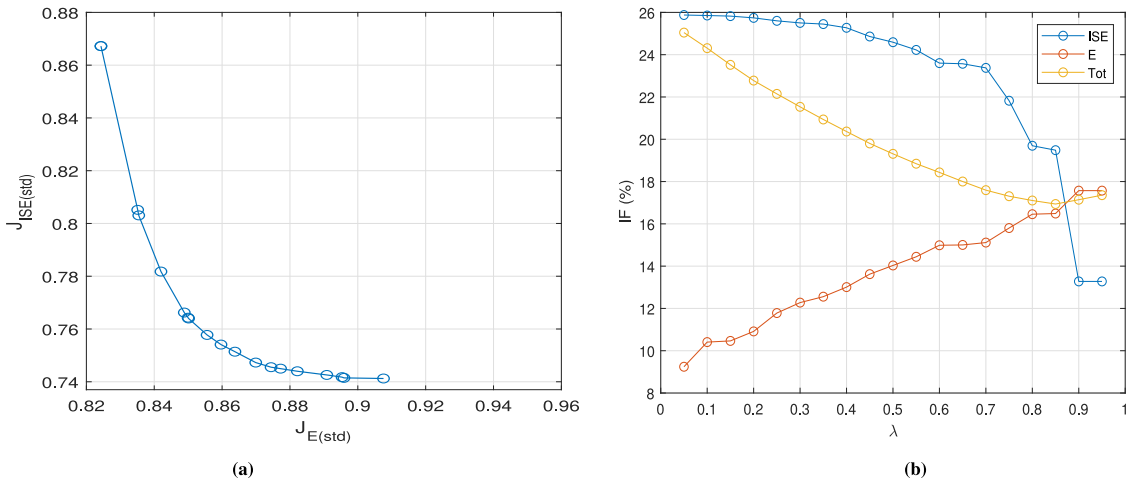

Fig. 5. (**a**) Pareto front of standardised integral squared error vs. standardised energy consumption. (**b**) Improvement factor vs. weighting factor.

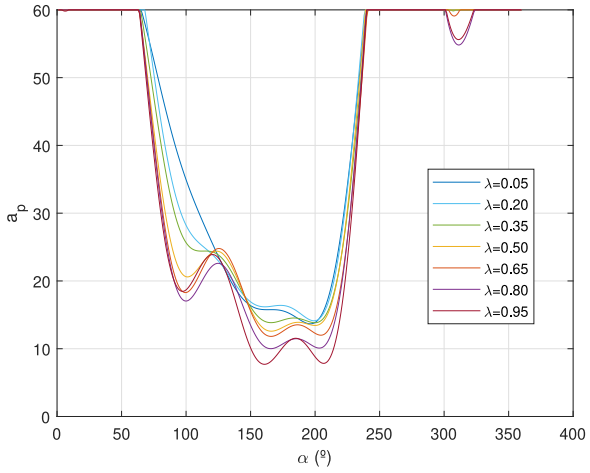

Fig. 6. Control actions obtained using control law (23)–(26) and coefficients θ (Table B.8) for different weighting factors with respect to the relative orientation of the vehicle (in degrees).

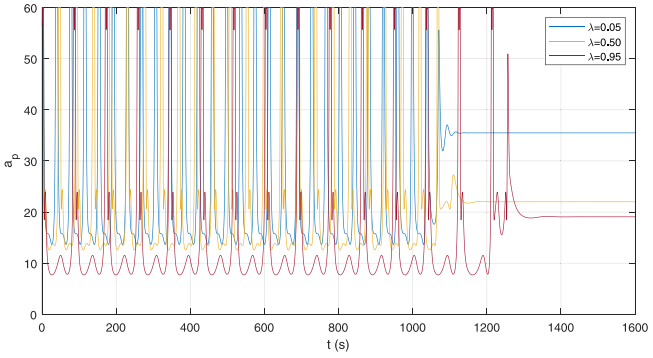

Fig. 7. Control actions using control law (23)–(26) and coefficients θ (Table B.8) for $\lambda = 0.05$, $\lambda = 0.50$ and $\lambda = 0.95$.

was set to 10 seconds, i.e., the control actions applied belong to the first 10 seconds of the sliding time window and the optimisation is carried out every 10 seconds.

The results of comparing MPC with the proposed control scheme are shown below.

The values of the time to reach the destination, the integral square error (J_{ISE}) and the energy (J_E) for a final simulation time of 1600s

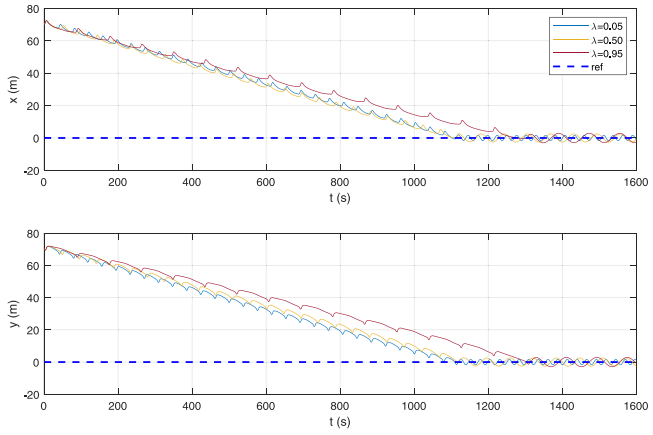

Fig. 8. Comparative graphs of progress on the X-axis and on the Y-axis obtained using the control law (23)–(26) and coefficients θ (Table B.8) for $\lambda = 0.05$, $\lambda = 0.50$ and $\lambda = 0.95$. The dark blue dashed line represents the coordinates of the recovery point.

Table 4
Comparison of the MPC scheme and the control law (23)–(26) for different weighting factors.

λ	Control law	Time (min)	J_{ISE} (m^{2}s)	J_E (J)
0.05	MPC	19.28	$3.8997 \cdot 10^7$	$5.6258 \cdot 10^4$
	Proposed[a]	18.48	$3.7879 \cdot 10^7$	$4.8772 \cdot 10^4$
0.50	MPC	21.75	$4.4730 \cdot 10^7$	$4.8088 \cdot 10^4$
	Proposed[a]	18.58	$3.8534 \cdot 10^7$	$4.6202 \cdot 10^4$
0.95	MPC	30.83	$6.0478 \cdot 10^7$	$4.4369 \cdot 10^4$
	Proposed[a]	21.33	$4.4293 \cdot 10^7$	$4.4303 \cdot 10^4$

[a] Control law (23)–(26), coefficients θ (Table B.8) for λ.

have been selected for comparison in Table 4. It can be observed that the results for the Fourier Series control scheme are better than for the MPC. Also notice that, in the energy consumption indicator, it is not considered the energy consumed by the computer onboard the AUV to calculate the control actions in the MPC approach (which is expected to be higher due to the intensive computational task).

The comparison of control actions, trajectories, and positions of the AUV for the weighting factors $\lambda = 0.05$, 0.50, 0.95 are shown in Figs. 9–11. It is interesting to note in Fig. 10 that the trajectories produced by MPC are qualitatively similar to those of the control (23)–(26), both approaching the target point in a spiral-like path, but the

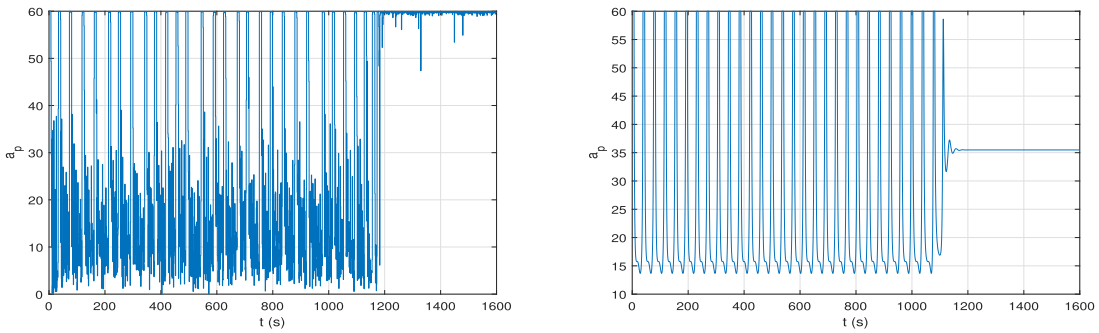

(a) MPC

(b) Fourier Series based control (23 - 26)

Fig. 9. Comparison of control actions obtained with the MPC and with the Fourier Series based control (23)–(26) for $\lambda = 0.05$.

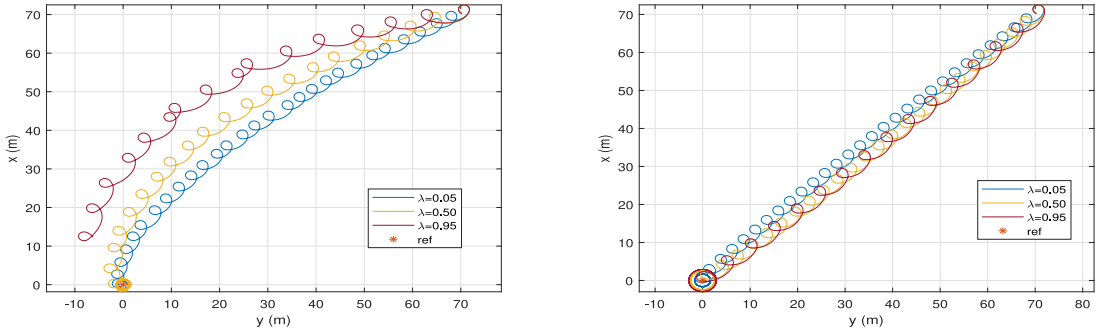

(a) MPC

(b) Fourier Series based control (23 - 26)

Fig. 10. Comparison of trajectories obtained with the MPC scheme and with the Fourier Series based control (23)–(26) for $\lambda = 0.05,\ 0.50,\ 0.95$. The red point represents the destination. (For interpretation of the references to colour in this figure legend, the reader is referred to the web version of this article.)

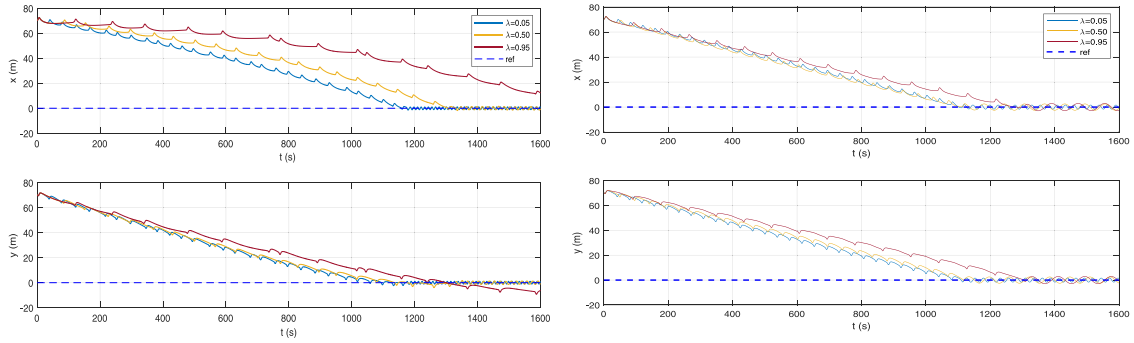

(a) MPC

(b) Fourier Series based control (23 - 26)

Fig. 11. Comparative graphs of progress on the X-axis and on the Y-axis obtained using the MPC scheme and the Fourier Series based control (23)–(26) for $\lambda = 0.05,\ 0.50,\ 0.95$. The dark blue dashed line represents the coordinates of the recovery point.

control actions obtained by the control (23)–(26) are smoother than those obtained by MPC, the trajectories are shorter spiral-like paths and looking at the x and y positions versus time graphs, it can be also seen that with the control (23)–(26) the AUV reaches the destination earlier.

In view of the previous results, the control (23)–(26) is more suitable to solve the problem posed. In addition, other disadvantages of the MPC scheme were also detected during the comparative analysis. The main issue with the MPC control scheme is that the optimisation procedure inherent to it requires computation times that may be too long to be used in real time. The closed loop implementation of the above strategy would require the computation of the optimal control actions at each sliding time window, which may be not feasible in practice. Furthermore, applying the MPC control scheme with a discrete time setting means that the optimal signal can be discontinuous, oscillating rapidly between the maximum and minimum values in a sampling period. This is undesirable for thruster operation and can damage the only remaining thruster.

In contrast, the control law proposed in this paper does not need online optimisation of the control actions since the parameters of the control law are optimised offline, and the algorithm only needs to recalculate the control action according to the relative angle between the AUV and the target point at each sampling time. As a consequence, computation times are negligible in practice, which further contributes to energy savings since there is no need to carry out an optimisation onboard the AUV. In addition, the control actions are smoother. Finally, the control law (23)–(26) needs less time and energy to reach the destination point than the MPC approach as shown in Table 4.

For these reasons, MPC and similar approaches are not suitable for the situation studied, and are discarded for the simulator tests presented in the following subsection.

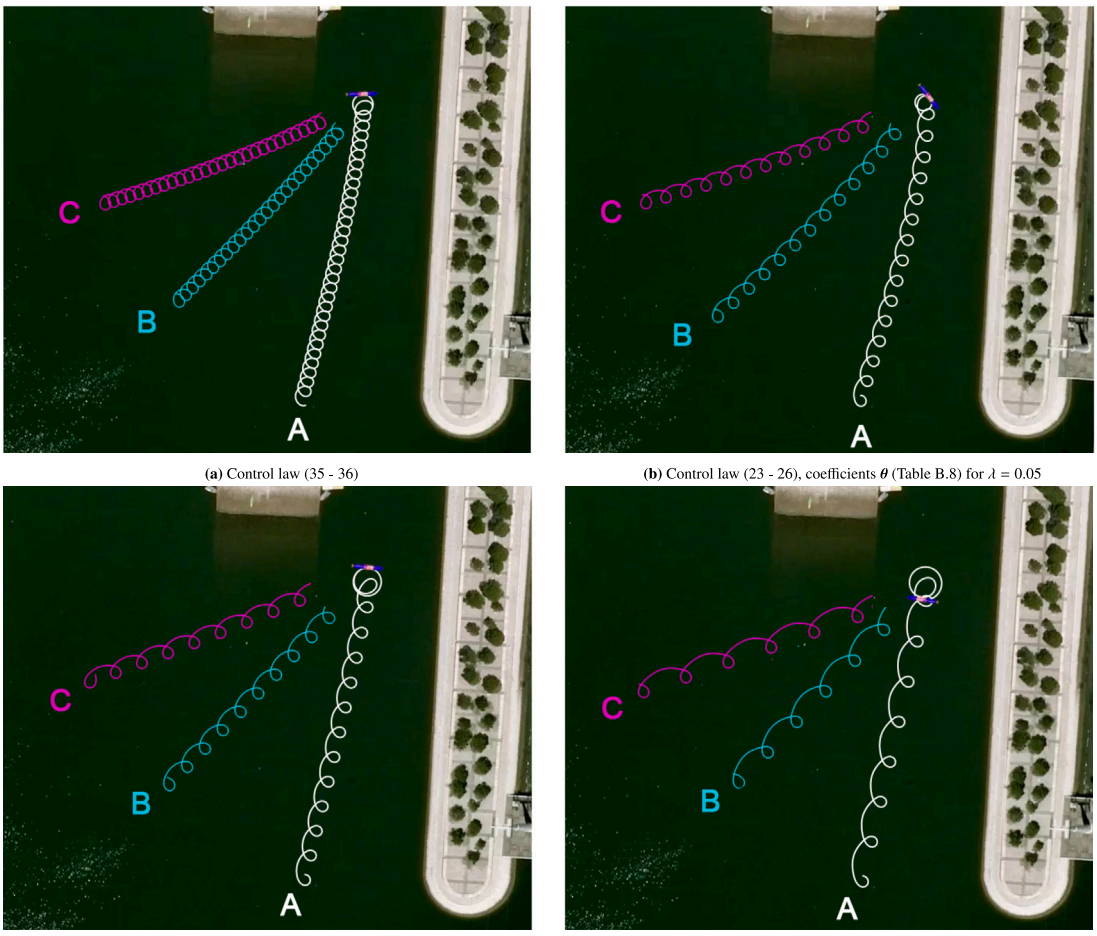

(a) Control law (35 - 36)

(b) Control law (23 - 26), coefficients $\boldsymbol{\theta}$ (Table B.8) for $\lambda = 0.05$

(c) Control law (23 - 26), coefficients $\boldsymbol{\theta}$ (Table B.8) for $\lambda = 0.50$

(d) Control law (23 - 26), coefficients $\boldsymbol{\theta}$ (Table B.8) for $\lambda = 0.95$

Fig. 12. Trajectories obtained from initial conditions A (White trajectory), B (Cyan trajectory) and C (Pink trajectory). (For interpretation of the references to colour in this figure legend, the reader is referred to the web version of this article.)

4.4. Simulation results

Several simulation tests have been carried out using the simulator developed by the DOSR-ISR group of the Instituto Superior Tecnico of Lisbon. This tool allows for more realistic and accurate simulations as it has more detailed and complete models of both MEDUSA and the environment. Once again, weighting factors $\lambda = 0.05$, $\lambda = 0.50$ and $\lambda = 0.95$ have been chosen for comparison. These tests consist on the one hand of sending the AUV from various initial conditions to the desired recovery area and on the other hand of testing the effect of constant currents in these same examples. The differences in trajectories, energy consumptions and times are analysed.

4.4.1. Effect of different initial conditions

The initial conditions and the desired recovery point are shown in Table 5.

Fig. 12(a) shows the trajectories, from the initial conditions in Table 5, obtained by reference control law (35)–(36). These trajectories are used as a reference to compare with the optimal solutions found for control law (23)–(26). It can be seen how these trajectories present the tightest loops.

Figs. 12(b), 12(c) and 12(d) illustrate the trajectories, from the same initial conditions, obtained with control law (23)–(26) and coefficients $\boldsymbol{\theta}$ (Table B.8) for $\lambda = 0.05$, $\lambda = 0.50$ and $\lambda = 0.95$, respectively. The trajectories in Fig. 12(b) focus more on reducing the ISE, and they reach the destination point earlier and consume more energy. For Fig. 12(c), equal weight to decreasing the ISE and the energy consumed is considered, so the trajectories are in between the trajectories for $\lambda = 0.05$ and $\lambda = 0.95$; they reach the destination point later than for $\lambda = 0.05$ but consume less energy; in contrast, they reach the destination point earlier than for $\lambda = 0.95$ but consume more energy. Finally, for Fig. 12(d), the trajectories focus on minimising energy consumption, they have the most separated loops, and are slower than trajectories for $\lambda = 0.05$ and $\lambda = 0.50$, specifically, about 180 seconds slower than for $\lambda = 0.05$. This latter value matches with the 200 seconds observed in the simulation tests of Section 4.2.

In practice, the results in Table 6 confirm that the trajectories in Fig. 12(a) are the slowest to reach the target point and the ones which consumes more energy. Therefore, the control law (23)–(26) and the coefficients $\boldsymbol{\theta}$ (Table B.8) for any λ improve the reference control law (35)–(36) described in Chaos et al. (2022).

Table 5
Coordinates of the initial conditions A, B, C and the recovery point F.

Point	x (m)	y (m)	ψ (rad)	u (m/s)	v (m/s)	r (rad/s)
A	−86	−19	$\pi/2$	0	0	0
B	−60	−55	$\pi/2$	0	0	0
C	−30	−75	$\pi/2$	0	0	0
F	0	0	–	–	–	–

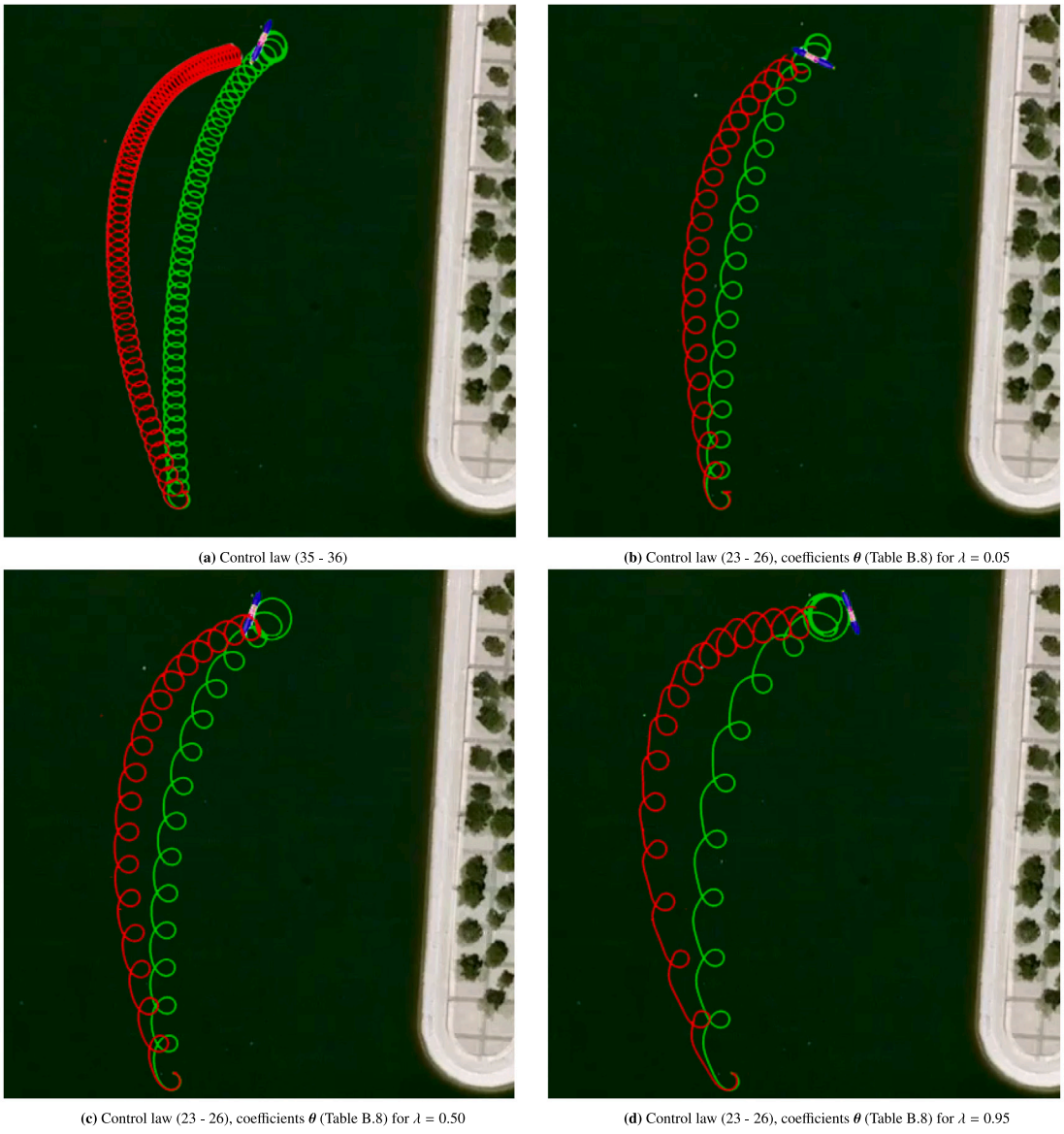

(a) Control law (35 - 36)

(b) Control law (23 - 26), coefficients $\boldsymbol{\theta}$ (Table B.8) for $\lambda = 0.05$

(c) Control law (23 - 26), coefficients $\boldsymbol{\theta}$ (Table B.8) for $\lambda = 0.50$

(d) Control law (23 - 26), coefficients $\boldsymbol{\theta}$ (Table B.8) for $\lambda = 0.95$

Fig. 13. Trajectories obtained from initial condition A and with currents $v_{c1} = 0.5 \cdot v_f$ (Green trajectory) and $v_{c2} = 0.9 \cdot v_f$ (Red trajectory). (For interpretation of the references to colour in this figure legend, the reader is referred to the web version of this article.)

If all trajectories are analysed from the point of view of the initial conditions, it can be observed that they do not influence the shape of the trajectory, the AUV reaches the recovery point sooner or later depending on whether it is closer or further away from the target, but the control law produces the same type of trajectory. Therefore, the control law is robust against changes in the initial conditions.

4.4.2. Trajectories in the presence of constant currents

In order to further test the robustness of control law (23)–(26), a constant unknown current with two different levels of intensity is introduced, as follows

$$v_{c1} = 0.5 \cdot v_f$$
$$v_{c2} = 0.9 \cdot v_f,$$

where $v_f = 6.62$ cm/s the average speed that the vehicle can reach under the control action obtained in Chaos et al. (2022). For the sake of clarity, and without loss of generality, the initial condition A is selected and a current in the Y-axis direction is considered. Then, Eq. (2) becomes:

$$\dot{y} = u \cdot \sin(\psi) + v \cdot \cos(\psi) - v_c$$

Trajectories in Fig. 13 undergo larger deviations with increasing current intensity.

5. Discussion

In view of the results obtained, the control law (23)–(26) is more suitable than the MPC control scheme to be implemented in the vehicle.

The improvement factor indicates that the energy cost function can improve up to 9% between $\lambda = 0.05$ and $\lambda = 0.95$, while the trajectory ISE cost function worsens by 13%. This means that the trajectory

Table 6
Time to reach the recovery point and energy consumption from different initial conditions.

Initial conditions	Control law	Time (min)	Energy consumption (J)
A	Reference[a]	17.87	$5.1327 \cdot 10^4$
(White trajectory)	[b] $\lambda = 0.05$	14.57	$4.8558 \cdot 10^4$
	[b] $\lambda = 0.50$	14.60	$4.5299 \cdot 10^4$
	[b] $\lambda = 0.95$	17.87	$4.3858 \cdot 10^4$
B	Reference[a]	16.10	$5.0728 \cdot 10^4$
(Cyan trajectory)	[b] $\lambda = 0.05$	12.97	$4.8443 \cdot 10^4$
	[b] $\lambda = 0.50$	13.05	$4.4990 \cdot 10^4$
	[b] $\lambda = 0.95$	15.83	$4.3687 \cdot 10^4$
C	Reference[a]	15.70	$5.0653 \cdot 10^4$
(Pink trajectory)	[b] $\lambda = 0.05$	12.42	$4.8194 \cdot 10^4$
	[b] $\lambda = 0.50$	12.73	$4.4981 \cdot 10^4$
	[b] $\lambda = 0.95$	15.62	$4.3548 \cdot 10^4$

[a] Reference control law (35)–(36) defined in Chaos et al. (2022).
[b] Control law (23)–(26), coefficients θ (Table B.8) for λ.

obtained from coefficients for $\lambda = 0.95$ takes about 180 seconds longer to reach the target than the trajectory for $\lambda = 0.05$, but saves 9% more energy. For $\lambda = 0.50$ a intermediate solution is found, the trajectory ISE cost function worsens by 1.4% with respect to $\lambda = 0.05$ solution, the energy cost function improves by 5%, and its trajectory takes about 30 seconds longer to reach the destination than for $\lambda = 0.05$ solution.

In addition, it has been verified that the initial conditions do not influence the behaviour of the control law.

Regarding the effect of the currents, it has been observed that current $v_{c1} = 0.5 \cdot v_f$ does not significantly affect trajectories for $\lambda = 0.05$, $\lambda = 0.50$ and $\lambda = 0.95$. However, current $v_{c2} = 0.9 \cdot v_f$ especially affects $\lambda = 0.95$ solution, since it takes much longer to reach the destination point than the other solutions (reference, $\lambda = 0.05$ and $\lambda = 0.50$) and also experiences a greater deviation.

In conclusion, energy savings are achieved at the cost of slightly reducing the improvement factor of the cost function with respect to the trajectory ISE, which is generally beneficial. The control signals obtained are sufficiently smooth and simple to be able to be implemented in the control of the real vehicle without requiring significant effort from the actuators.

Taking all this into consideration, the control laws for each series of coefficients θ for the different weighting factors could be used within the fault-tolerant system to adapt the control depending on the energy available in the batteries. Another possible strategy is not to adapt the control and set certain coefficients depending on a specific objective, such as selecting the coefficients for $\lambda = 0.50$ if the goal is to promote both vehicle movement and energy savings or if the vehicle has to deal with a strong current, or those for $\lambda = 0.95$ if the aim is to reduce energy consumption as much as possible and if time to reach the target is secondary.

A future line of research will include an obstacle collision avoidance system in the controller, given that in this work it has been assumed that it is possible to move directly towards the recovery zone without any obstacle in the way. In addition, the proposed control law will be tested in the specific real environment upon which the simulations presented in this paper were based. In a practical application, a function should be defined so that based on the amount of energy available in the batteries, it would assign the different weighting factors and apply their corresponding coefficients θ.

6. Conclusions

An optimal fault-tolerant control law considering the minimal integral square error of the vehicle's trajectory and the lowest possible energy consumption of the batteries for an underactuated AUV has been analysed and designed. The extreme case of thruster's failure which leaves only one stern horizontal thruster available to drive the AUV from a initial condition to a desired recovery area, i.e. to execute an automatic homing manoeuvre, has been considered.

The stability of the proposed control law and the convergence of the trajectory to a neighbourhood of the desired recovery area from any initial condition has been demonstrated analytically.

The optimal fault-tolerant control has been defined as a control law that is a function of the relative orientation of the AUV with respect to the destination. This control law is represented from a Fourier series of order 5, whose coefficients have been optimised using genetic algorithm and considering a weighting factor to balance between ISE and energy consumption.

A comparison between the proposed control scheme and MPC scheme has been made. The proposed control scheme has resulted the most suitable to implement in the vehicle.

The Pareto front showed the trade-off solutions that can be obtained for the different weighting factors. The solutions obtained for $\lambda = 0.05$, $\lambda = 0.50$ and $\lambda = 0.95$ have been studied in depth by means of further simulations. Two types of tests have been carried out. On the one hand, the AUV was driven from several initial conditions to the desired recovery area. On the other hand, the effect of constant currents was tested. It has been proven that the optimal control law proposed is robust enough against changes in the initial conditions, and the effect of constant currents. In general, the fastest trajectories are achieved for $\lambda = 0.05$, the greatest energy savings occur for $\lambda = 0.95$, and for $\lambda = 0.50$ an intermediate solution is presented. Therefore, this results show that the control law can be used in a real scenario within the fault-tolerant system to adapt the control depending on the energy available in the batteries.

CRediT authorship contribution statement

Cristina Cerrada: Writing – review & editing, Writing – original draft, Visualization, Validation, Software, Resources, Methodology, Investigation, Formal analysis, Data curation, Conceptualization. **Dictino Chaos:** Writing – review & editing, Writing – original draft, Visualization, Validation, Software, Resources, Methodology, Investigation, Formal analysis, Data curation, Conceptualization. **David Moreno-Salinas:** Writing – review & editing, Writing – original draft, Visualization, Validation, Software, Resources, Methodology, Investigation, Formal analysis, Data curation, Conceptualization. **António Pascoal:** Writing – review & editing, Supervision, Funding acquisition. **Joaquín Aranda:** Writing – review & editing, Supervision, Project administration, Funding acquisition.

Declaration of competing interest

The authors declare the following financial interests/personal relationships which may be considered as potential competing interests: One of the authors, António Pascoal, serves as Guest Editor of the Special Issue Marine Navigation Control.

Appendix A

A summary of the variables used to describe the control law and the problem formulation in Section 2.2, and used in the demonstration of Section 3 are shown in Table A.7.

Appendix B

The optimal coefficients θ^* of the Fourier series that define the control law (23)–(26), obtained for each value of the weighting factor λ, are presented in Table B.8.

Table A.7
List of variables used in Sections 2.2 and 3.

Symbol	Description
$\chi = [x, y, \psi, u, v, r]^T$, $\dot{\chi} = f(\chi, a_p)$	Vehicle state (position, orientation and speeds) and its temporal derivative
θ, θ^*	Coefficients of the control law, and their optimal values
χ_0, Ω, R_0, $\boldsymbol{X_r} = [x_r, y_r]^T$, Ω_r, R_f	Initial condition of the AUV and its neighbourhood, radius that defines the area of initial conditions, coordinates of the reference point, neighbourhood of $\boldsymbol{X_r}$ and radius defining the neighbourhood of $\boldsymbol{X_r}$
J_{Tot}, J_{ISE}, J_E	Cost function: total, referred to the error of the vehicle's trajectory and to energy consumption
λ	Weighting factor
α	Relative orientation of the AUV with respect $\boldsymbol{X_r}$
ΔT, T_f, t_f	Sampling period, end time and time to reach $\boldsymbol{X_r}$
i, n	Sample number and final number of samples
N, $[b_0; b_j; c_j]$	Order and coefficients of Fourier series
P, I_p, I_s	Instantaneous electrical power consumption and current drawn by thrusters
$\mathcal{R}_a$, K_e	Thruster's resistance and electrical constant
P_p	Constant power required by the on-board computers
n_p, n_s	Rotational velocity of the thrusters (rps)
n_{max}	Rotational velocity at maximum continuous torque (rps)
w_p	Propeller rotational velocity (rad/s)
Q_p, K_t	Propeller torque and torque constant
ρ, b	Seawater density close to surface and viscous friction coefficient
R_p, d_p	Radius and diameter of propeller
v_{a_p}, v_{p_p}	Propeller's advance and lateral velocity
$l' = [l_x, l_y]$	Distance from the centre of propeller to vehicle's centre of mass
β_p, γ_p, ζ_p	Advance angle, angle of attack and pitch angle of the propeller
C_Q, k_1, k_2, C_L^L, C_D^L, C_L^{max}, C_D^{max}, C_D^{min}, o_L, o_D	Parameters of the model of energy consumed by the thrusters
a_0, Δa, $\Delta\psi$	Parameters of control law (35)–(36): constant value, magnitude of the change of the control signal and angle correction
$IF_{Tot,ISE,E}$	Improvement factor: total, referred to the error of the vehicle's trajectory and to energy consumption
V_{max}, r_{min}, r_{max}	Bounds of linear and angular velocity
$a_{p_{ref}}$, $a_{p_{FS}}$	Reference control law and control law as a function of the relative orientation of the vehicle with respect to the recovery point described as a Fourier series
κ, m, m', ϵ_1, ϵ_2, δ_1, δ_2, δ_3	Positive constants
L_c	Lipschitz constant
$R(t)$, R_1, R_2, R_{min}	Different radii for neighbourhoods of $\boldsymbol{X_r}$
t^*, dt_1, dt_2	Different time instants during the switching of the control action

Table B.8
Optimal coefficients of the Fourier series with $N = 5$ for the different weighting factors.

λ	b0	b1	c1	b2	c2	b3	c3	b4	c4	b5	c5
0.05	100.53	29.09	−12.70	−8.38	4.05	3.68	5.24	3.48	−6.56	−2.62	−3.14
0.10	100.53	29.09	−14.05	−8.55	4.05	3.68	6.25	3.48	−7.45	−2.62	−4.40
0.15	100.53	29.09	−14.32	−8.63	4.05	3.68	6.82	3.48	−6.56	−2.62	−3.85
0.20	101.33	27.42	−14.66	−12.57	7.64	−0.39	12.04	1.68	−4.73	−3.43	−4.20
0.25	101.33	27.42	−14.66	−12.57	7.64	−0.39	12.04	−0.32	−5.07	−3.43	−5.75
0.30	99.46	29.25	−14.95	−9.13	5.04	2.62	9.49	3.48	−6.56	−2.11	−5.68
0.35	99.46	29.25	−15.78	−9.32	4.36	2.62	9.49	3.48	−6.56	−2.44	−6.43
0.40	98.85	29.25	−15.30	−9.06	5.04	1.89	10.40	2.21	−6.68	−2.91	−6.78
0.45	99.46	29.25	−17.96	−9.39	4.47	2.62	11.37	2.63	−6.68	−2.91	−6.78
0.50	99.46	29.25	−17.99	−9.78	5.04	2.62	11.68	2.10	−6.68	−3.43	−7.63
0.55	98.29	29.25	−18.33	−10.21	3.45	1.79	11.44	2.31	−6.68	−3.06	−8.27
0.60	97.36	29.25	−17.99	−10.21	4.22	1.79	12.74	2.40	−6.68	−3.43	−8.87
0.65	97.36	29.25	−17.99	−10.21	4.22	1.79	12.75	2.31	−6.68	−3.43	−8.87
0.70	97.36	29.25	−17.99	−10.21	4.22	1.79	14.25	2.40	−5.40	−3.43	−9.09
0.75	95.95	29.25	−17.99	−10.21	7.20	1.79	14.84	2.40	−5.40	−3.43	−7.34
0.80	95.95	29.25	−17.99	−11.95	7.20	1.79	15.89	2.82	−5.40	−3.43	−8.34
0.85	95.95	29.25	−17.99	−11.95	7.20	1.79	15.84	2.53	−5.40	−3.43	−8.27
0.90	94.75	29.25	−17.99	−13.89	7.20	0.99	16.53	2.53	−4.73	−5.39	−8.87
0.95	94.75	29.25	−17.99	−13.89	7.20	0.99	16.53	2.53	−4.73	−5.39	−8.87

References

Abreu, P. C., Botelho, J., Góis, P., Pascoal, A., Ribeiro, J., Ribeiro, M., Rufino, M., Sebastião, L., & Silva, H. (2016). The MEDUSA class of autonomous marine vehicles and their role in EU projects. In *OCEANS 2016 - Shanghai* (pp. 1–10). http://dx.doi.org/10.1109/OCEANSAP.2016.7485620.

Aguiar, A. P., & Pascoal, A. M. (2001). Regulation of a nonholonomic autonomous underwater vehicle with parametric modeling uncertainty using Lyapunov functions. In *Decision and control, 2001. Proceedings of the 40th IEEE conference on, vol. 5* (pp. 4178–4183). http://dx.doi.org/10.1109/.2001.980841.

Ahmadzadeh, S. R., Leonetti, M., Carrera, A., Carreras, M., Kormushev, P., & Caldwell, D. G. (2014). Online discovery of AUV control policies to overcome thruster failures. In *2014 IEEE international conference on robotics and automation* (pp. 6522–6528). [ISSN: 1050-4729] http://dx.doi.org/10.1109/ICRA.2014.6907821.

Amin, A. A., & Hasan, K. M. (2019). A review o Fault Tolerant Control Systems: Advancements and applications. *Measurement*, *143*, 58–68. http://dx.doi.org/10.1016/j.measurement.2019.04.083.

Baldini, A., Ciabattoni, L., Felicetti, R., Ferracuti, F., Freddi, A., & Monterìù, A. (2018). Dynamic surface fault tolerant control for underwater remotely operated vehicles. *ISA Transactions*, *78*, 10–20. http://dx.doi.org/10.1016/j.isatra.2018.02.021.

Bashir, A., Khan, S., Iqbal, N., Bashmal, S., Ullah, S., Fayyaz, & Usman, M. (2023). A review of the various control algorithms for trajectory control of unmanned underwater vehicles. *Sustainability*, *15*, Article 14691. http://dx.doi.org/10.3390/su152014691.

Cerrada, C., Chaos, D., Moreno-Salinas, D., & Aranda, J. (2023). Optimal control law of an AUV using a single thruster. *Revista Iberoamericana de Automática e Informática industrial*, http://dx.doi.org/10.4995/riai.2023.19034.

Chaos, D., Moreno-Salinas, D., & Aranda, J. (2022). Fault-tolerant control for AUVs using a single thruster. *IEEE Access*, *10*, 22123–22139. http://dx.doi.org/10.1109/ACCESS.2022.3152190.

Corradini, M. L., Monteriu, A., & Orlando, G. (2011). An actuator failure tolerant control scheme for an underwater remotely operated vehicle. *IEEE Transactions on Control Systems Technology*, *19*, 1036–1046. http://dx.doi.org/10.1109/TCST.2010.2060199.

Crasta, N., Moreno-Salinas, D., Pascoal, A. M., & Aranda, J. (2018). Multiple autonomous surface vehicle motion planning for cooperative range-based underwater target localization. *Annual Reviews in Control*, *46*, 326–342. http://dx.doi.org/10.1016/j.arcontrol.2018.10.004.

Ding, X., & Zhu, D. (2020). Research on static fault-tolerant control method of UUV based on MPC in two dimension. In *2020 Chinese control and decision conference* (pp. 5333–5338). http://dx.doi.org/10.1109/CCDC49329.2020.9164413.

Fossen, T. I. (2002). *Marine control systems: Guidance, navigation and control of ships, rigs and underwater vehicles*. Trondheim: Marine Cybernetics AS.

Ghabcheloo, R., Aguiar, A. P., Pascoal, A., Silvestre, C., Kaminer, I., & Hespanha, J. (2009). Coordinated path-following in the presence of communication losses and time delays. *SIAM Journal on Control and Optimization*, *48*, 234–265. http://dx.doi.org/10.1137/060678993.

Glaviano, F., Esposito, R., Cosmo, A. D., Esposito, F., Gerevini, L., Ria, A., Molinara, M., Bruschi, P., Costantini, M., & Zupo, V. (2022). Management and sustainable exploitation of marine environments through smart monitoring and automation. *Journal of Marine Science and Engineering*, *10*, 297. http://dx.doi.org/10.3390/jmse10020297.

Gong, J., Jiang, Y., & Xu, W. (2014). *Model predictive control for self-driving vehicles*. Beijing, China: Beijing Institute of Technology Press.

Hao, L. -Y., Zhang, Y. -Q., & Li, H. (2021). Fault-tolerant control via integral sliding mode output feedback for unmanned marine vehicles. *Applied Mathematics and Computation*, *401*, Article 126078. http://dx.doi.org/10.1016/j.amc.2021.126078.

Häusler, A. J. (2015). *Mission planning for multiple cooperative robotic vehicles* (Ph.D. thesis), UNIVERSIDADE DE LISBOA INSTITUTO SUPERIOR TÉCNICO.

Hou, C., Li, X., Wang, H., Zhai, P., & Lu, H. (2022). Fuzzy linear extended states observer-based iteration learning fault-tolerant control for autonomous underwater vehicle trajectory-tracking system. *IET Control Theory & Applications*, http://dx.doi.org/10.1049/cth2.12288.

Hung, N. T., Crasta, N., Moreno-Salinas, D., Pascoal, A. M., & Johansen, T. A. (2020). Range-based target localization and pursuit with autonomous vehicles: An approach using posterior CRLB and model predictive control. *Robotics and Autonomous Systems*, *132*, Article 103608. http://dx.doi.org/10.1016/j.robot.2020.103608.

Hung, N. T., & Pascoal, A. M. (2018). Cooperative path following of autonomous vehicles with model predictive control and event triggered communications. In *6th IFAC conference on nonlinear model predictive control NMPC 2018*: *IFAC-PapersOnLine*, In *6th IFAC conference on nonlinear model predictive control NMPC 2018*: *51*, 562–567.http://dx.doi.org/10.1016/j.ifacol.2018.11.031,

Kroese, D. P., Brereton, T., Taimre, T., & Botev, Z. I. (2014). Why the Monte Carlo method is so important today. *WIREs Computational Statistics*, *6*, 386–392. http://dx.doi.org/10.1002/wics.1314.

Lv, T., Zhou, J., Wang, Y., Gong, W., & Zhang, M. (2020). Sliding mode based fault tolerant control for autonomous underwater vehicle. *Ocean Engineering*, *216*, Article 107855. http://dx.doi.org/10.1016/j.oceaneng.2020.107855.

Mondal, K., & Banerjee, T. (2019). Autonomous underwater vehicles: Recent developments and future prospects. *International Journal for Research in Applied Science and Engineering Technology*, *7*, 215–222. http://dx.doi.org/10.22214/ijraset.2019.11036.

Moreno-Salinas, D., Pascoal, A., & Aranda, J. (2016). Optimal sensor placement for acoustic underwater target positioning with range-only measurements. *IEEE Journal of Oceanic Engineering*, *41*, 620–643.

Pearson, A. R., Sutton, R., Burns, R. S., & Robinson, P. (2001). A fuzzy fault tolerant control scheme for an autonomous underwater vehicle. *IFAC Proceedings Volumes*, *34*, 425–430. http://dx.doi.org/10.1016/S1474-6670(17)35119-4.

Pedro, M., Moreno-Salinas, D., Crasta, N., & Pascoal, A. (2015). Underwater single-beacon localization: Optimal trajectory planning and minimum-energy estimation. *IFAC-PapersOnLine*, *48*, 155–160. http://dx.doi.org/10.1016/j.ifacol.2015.06.025.

Pinto, J., Costa, M., Lima, K., Dias, P., Pereira, J., Ribeiro, M., Campos, R., Mirmalek, Z., Mendes, R., Castejón, F. L., Gilabert, J., Tomasino, M. P., Magalhães, C., da Silva, J. C. B., Relvas, P., Lukaczyk, T., Skarpnes, K. A., Ludvigsen, M., Chekalyuk, A., ... Rajan, K. (2021). To boldly dive where no one has gone before: Experiments in coordinated robotic ocean exploration. In B. Siciliano, C. Laschi, & O. Khatib (Eds.), *Springer proceedings in advanced robotics*, *Experimental robotics* (pp. 472–487). Cham: Springer International Publishing, http://dx.doi.org/10.1007/978-3-030-71151-1_42.

Podder, T. K., & Sarkar, N. (2001). Fault-tolerant control of an autonomous underwater vehicle under thruster redundancy. *Robotics and Autonomous Systems*, *34*, 39–52. http://dx.doi.org/10.1016/S0921-8890(00)00100-7.

Pugi, L., Allotta, B., & Pagliai, M. (2018). Redundant and reconfigurable propulsion systems to improve motion capability of underwater vehicles. *Ocean Engineering*, *148*, 376–385. http://dx.doi.org/10.1016/j.oceaneng.2017.11.039.

Rauber, J. G., Santos, C. H. F. d., Chiella, A. C. B., & Motta, L. R. H. (2012). A strategy for thruster fault-tolerant control applied to an AUV. In *2012 17th international conference on methods models in automation robotics* (pp. 184–189).

Saback, R., Cesar, D., Arnold, S., Lepikson, H., Santos, T., & Albiez, J. (2016). Fault-tolerant control allocation technique based on explicit optimization applied to an autonomous underwater vehicle. In *OCEANS 2016 MTS/IEEE Monterey* (pp. 1–8). http://dx.doi.org/10.1109/OCEANS.2016.7761251.

Sarkar, M., Nandy, S., & Shome, S. N. (2015). Energy efficient trajectory tracking controller for underwater applications: A robust approach. *Aquatic Procedia*, *4*, 571–578. http://dx.doi.org/10.1016/j.aqpro.2015.02.074.

Sarkar, M., Nandy, S., Vadali, S. R. K., Roy, S., & Shome, S. N. (2016). Modelling and simulation of a robust energy efficient AUV controller. *Mathematics and Computers in Simulation*, *121*, 34–47. http://dx.doi.org/10.1016/j.matcom.2015.08.021.

Sarkar, N., Podder, T. K., & Antonelli, G. (2002). Fault-accommodating thruster force allocation of an AUV considering thruster redundancy and saturation. *IEEE Transactions on Robotics and Automation*, *18*, 223–233.

SNAME (1950). *Nomenclature for Treating the Motion of a Sumerged Body Through a Fluid: Technical Report*, The Society of naval Architects and Marine Engineers, Technical and research bulletin N° 3-47.

Tian, Q., Wang, T., Liu, B., & Ran, G. (2022). Thruster fault diagnostics and fault tolerant control for autonomous underwater vehicle with ocean currents. *Machines*, *10*, 582. http://dx.doi.org/10.3390/machines10070582.

Tolstov, G. P., & Silverman, R. A. (1976). *Fourier series*. Dover Publications, Inc..

Wang, Y., Jiang, B., Wu, Z., Xie, S., & Peng, Y. (2020). Adaptive sliding mode fault-tolerant fuzzy tracking control with application to unmanned marine vehicles. *IEEE Transactions on Systems, Man, and Cybernetics, Part A: Systems and Humans*, 1–10. http://dx.doi.org/10.1109/TSMC.2020.2964808.

Wang, S., Jin, H., Meng, L., & Li, G. (2016). Optimize motion energy of AUV based on LQR control strategy. In *2016 35th Chinese control conference* (pp. 4615–4620). [ISSN: 1934-1768] http://dx.doi.org/10.1109/ChiCC.2016.7554068.

Wang, X., Wang, Y., Wang, P., Niu, W., Yang, S., & Luo, C. (2023). Sailing efficiency optimization and experimental validation of a Petrel long-range autonomous underwater vehicle. *Ocean Engineering*, *281*, Article 114604. http://dx.doi.org/10.1016/j.oceaneng.2023.114604.

Xia, Y., Xu, K., Huang, Z., Wang, W., Xu, G., & Li, Y. (2022). Adaptive energy-efficient tracking control of a X rudder AUV with actuator dynamics and rolling restriction. *Applied Ocean Research*, *118*, Article 102994. http://dx.doi.org/10.1016/j.apor.2021.102994.

Yang, Y., Xiao, Y., & Li, T. (2021). A survey of autonomous underwater vehicle formation: Performance, formation control, and communication capability. *IEEE Communications Surveys & Tutorials*, *23*, 815–841. http://dx.doi.org/10.1109/COMST.2021.3059998.

Yao, F., Yang, C., Zhang, M., & Wang, Y. (2019). Optimization of the energy consumption of depth tracking control based on model predictive control for autonomous underwater vehicles. *Sensors*, *19*, 162. http://dx.doi.org/10.3390/s19010162.

Zhang, H., & Zhu, D. (2021). Quantum-behaved particle swarm optimization fault-tolerant control for human occupied vehicle. In X.-J. Liu, Z. Nie, J. Yu, F. Xie, & R. Song (Eds.), *Lecture notes in computer science*, *Intelligent robotics and applications* (pp. 628–637). Cham: Springer International Publishing, http://dx.doi.org/10.1007/978-3-030-89092-6_57.